

A remote sensing technique for global monitoring of power plant CO₂ emissions from space and related applications

H. Bovensmann¹, M. Buchwitz¹, J. P. Burrows¹, M. Reuter¹, T. Krings¹, K. Gerilowski¹, O. Schneising¹, J. Heymann¹, A. Tretner², and J. Erzdinger²

¹Institute of Environmental Physics (IUP), University of Bremen FB1, Otto Hahn Allee 1, 28334 Bremen, Germany

²Helmholtz Centre Potsdam – GFZ German Research Centre for Geosciences, Telegrafenberg, 14473 Potsdam, Germany

Received: 6 November 2009 – Published in Atmos. Meas. Tech. Discuss.: 7 January 2010

Revised: 14 June 2010 – Accepted: 15 June 2010 – Published: 1 July 2010

Abstract. Carbon dioxide (CO₂) is the most important anthropogenic greenhouse gas (GHG) causing global warming. The atmospheric CO₂ concentration increased by more than 30% since pre-industrial times – primarily due to burning of fossil fuels – and still continues to increase. Reporting of CO₂ emissions is required by the Kyoto protocol. Independent verification of reported emissions, which are typically not directly measured, by methods such as inverse modeling of measured atmospheric CO₂ concentrations is currently not possible globally due to lack of appropriate observations. Existing satellite instruments such as SCIAMACHY/ENVISAT and TANSO/GOSAT focus on advancing our understanding of natural CO₂ sources and sinks. The obvious next step for future generation satellites is to also constrain anthropogenic CO₂ emissions. Here we present a promising satellite remote sensing concept based on spectroscopic measurements of reflected solar radiation and show, using power plants as an example, that strong localized CO₂ point sources can be detected and their emissions quantified. This requires mapping the atmospheric CO₂ column distribution at a spatial resolution of 2×2 km² with a precision of 0.5% (2 ppm) or better. We indicate that this can be achieved with existing technology. For a single satellite in sun-synchronous orbit with a swath width of 500 km, each power plant (PP) is overflown every 6 days or more frequent. Based on the MODIS cloud mask data product we conservatively estimate that typically 20 sufficiently cloud free overpasses per PP can be achieved every year. We found that for typical wind speeds in the range of 2–6 m/s the statistical uncertainty of the retrieved

PP CO₂ emission due to instrument noise is in the range 1.6–4.8 MtCO₂/yr for single overpasses. This corresponds to 12–36% of the emission of a mid-size PP (13 MtCO₂/yr). We have also determined the sensitivity to parameters which may result in systematic errors such as atmospheric transport and aerosol related parameters. We found that the emission error depends linearly on wind speed, i.e., a 10% wind speed error results in a 10% emission error, and that neglecting enhanced aerosol concentrations in the PP plume may result in errors in the range 0.2–2.5 MtCO₂/yr, depending on PP aerosol emission. The discussed concept has the potential to contribute to an independent verification of reported anthropogenic CO₂ emissions and therefore could be an important component of a future global anthropogenic GHG emission monitoring system. This is of relevance in the context of Kyoto protocol follow-on agreements but also allows detection and monitoring of a variety of other strong natural and anthropogenic CO₂ and CH₄ emitters. The investigated instrument is not limited to these applications as it has been specified to also deliver the data needed for global regional-scale CO₂ and CH₄ surface flux inverse modeling.

1 Introduction

Carbon dioxide (CO₂) is the most important anthropogenic greenhouse gas (GHG) and its atmospheric concentration increased by more than 30% since pre-industrial times and still continues to increase primarily due to burning of fossil fuels (IPCC, 2007; Canadell et al., 2007). Power plants, most notably coal-fired power plants, are among the largest CO₂ emitters (DoE and EPA, 2000). Coal-fired power plants (PPs) not only emit CO₂ in large quantities but also a number of



Correspondence to: M. Buchwitz
(michael.buchwitz@iup.physik.uni-bremen.de)

other constituents such as aerosols and ozone precursors and mercury with significant adverse influence on air quality and climate (Shindell and Faluvegi, 2010). As the world coal reserves are estimated at 930 Gt coal (see Shindell and Faluvegi, 2010, and references given therein), it can be expected that CO₂ emissions of coal-fired PPs will continue for many decades – probably with significantly growing emissions as the construction of coal-fired PPs is increasing rapidly for example in China and India (Shindell and Faluvegi, 2010).

In many countries national legislation requires regular reporting of CO₂ emissions (e.g., DoE and EPA, 2000). Emission reporting is also required by the Kyoto protocol (<http://unfccc.int/resource/docs/convkp/kpeng.pdf>). Current CO₂ emission reporting is mostly based on economical and technical information (e.g., amount and type of fuel burned, PP thermal efficiencies, CO₂ conversion factors) (DoE and EPA, 2000) but typically not on directly measured CO₂ emissions. Also required by the Kyoto protocol is independent verification of the reported emissions – a requirement difficult to be met globally due to lack of appropriate observations. The uncertainty of the reported anthropogenic CO₂ emissions varies by sector and country. They are assumed to vary on average by about 3–5% for the USA to 15–20% for China (Gregg et al., 2008), which became the largest national source of CO₂ emissions during 2006. Ackermann and Sundquist (2008) compared PP emission data bases and found that the absolute difference of the emissions of individual coal-fired PPs in the USA is typically about 20%. They conclude that several independent approaches are needed to reliably estimate how much CO₂ individual PPs emit. To improve global emission monitoring and reporting the use of satellites has been recommended (NRC, 2010). Currently however this is not possible as none of the existing or planned satellites has been specified for such an application.

Knowledge about the distribution and strength of individual strong emission sources is also very relevant to better constrain the separation of sources and sinks in the Northern Hemisphere. For example, the most recent estimates of EU fossil fuel emissions for 2000 are an order of magnitude larger than the European ecosystem carbon sink (Ciais et al., 2010). As a result even small uncertainties in the budget and the distribution of fossil fuel emission sources introduce substantial errors in the overall carbon budget derived from atmospheric inversions, when spatial resolution is increased from continental to regional, national or urban carbon scales.

Thus in spite of the current knowledge of the magnitude and distribution of fossil fuel combustion from inventories in Europe, there is clear need for much more accurate knowledge about the magnitude and the temporal and spatial variability of the anthropogenic emissions. For other countries and continents a similar or even worse situation is expected. This is recognised by the International Geosphere-Biosphere Program (IGBP) Global Emissions Inventory Activity (GEIA) project (<http://www.geiacenter.org/>) and this is one important motivation of research groups to produce high

resolution fossil fuel maps (Gurney et al., 2009; Rayner et al., 2010; Ciais et al., 2010; Oda and Maksyutov, 2010).

It has already been recognized that global satellite observations of the CO₂ vertical column (in molecules/cm²) or of the CO₂ dry air column-averaged mole fraction (in ppm), denoted XCO₂, has the potential to significantly advance our knowledge of regional natural CO₂ surface sources and sinks provided the satellite measurements have sufficiently high sensitivity to the planetary boundary layer (PBL), where the source/sink signal is largest, and are precise and accurate enough (Rayner and O'Brien, 2001; Houweling et al., 2004; Miller et al., 2007; Chevallier et al., 2007; Baker et al., 2010; Bréon and Ciais, 2010).

Existing or planned satellite instruments for measuring greenhouse gases with high near-surface sensitivity such as SCIAMACHY on ENVISAT (Burrows et al., 1995; Bovensmann et al., 1999), Orbiting Carbon Observatory (OCO) (Crisp et al., 2004) or TANSO on the Greenhouse Gases Observing Satellite (GOSAT) (Hamazaki et al., 2004; Kuze et al., 2009) (see Sect. 2 for details) aim primarily at providing additional constraints on natural CO₂ sources and sinks. None of the existing satellite CO₂ sensors has been designed to monitor anthropogenic CO₂ emissions. In this study we present first detailed results concerning the potential to monitor strong anthropogenic CO₂ emission sources such as coal-fired PPs from space. The investigated satellite mission and instrument, in the following referred to as “Carbon Monitoring Satellite” (CarbonSat), is based on the heritage of SCIAMACHY, OCO and GOSAT, but with additional capabilities such as wide swath imaging.

The overall scientific objectives of CarbonSat are similar to the objectives of GOSAT and OCO (OCO for CO₂ only), namely to provide XCO₂ and XCH₄ data products with a precision, accuracy and coverage needed for the quantification of regional-scale CO₂ and CH₄ surface fluxes. In contrast to OCO, CarbonSat also covers absorption bands of CH₄, a very potent greenhouse gas. To also observe atmospheric methane over water, e.g., in vulnerable northern high latitude regions such as the region west of Spitsbergen (Westbrook et al., 2009) or the East Siberian Arctic Shelf area (Shakhova et al., 2010), CarbonSat will use a dedicated sun-glint observation mode. These aspects will however not be discussed in this manuscript. Here we focus on one application, namely on the monitoring of PP CO₂ emissions.

The manuscript is organized as follows: In Sect. 2 we present a short overview about existing and planned GHG observing satellites. In Sect. 3 we present simulations and initial airborne observations of PP CO₂ emission plumes and discuss implications for the proposed satellite mission CarbonSat. In Sect. 4 we present the CarbonSat mission concept. The core of this manuscript is Sect. 5 where Observing System Simulation Experiments (OSSE) are described which have been conducted to quantify the impact of various error sources on the inferred emissions. The OSSE comprise radiative transfer and instrument simulations (Sect. 5.1), CO₂

retrievals based on synthetic radiances (Sect. 5.2), and estimates of random and systematic errors of the retrieved PP CO₂ emissions (Sect. 5.3). Clouds are an issue for the satellite observations discussed here. Therefore clear sky statistics are presented and discussed in Sect. 6. In Sect. 7 we shortly discuss the capability of CarbonSat to detect and quantify the emissions of other localized GHG sources including methane sources. A summary of the results obtained in this study and final conclusions are given in Sect. 8.

2 Status CO₂ and CH₄ observing satellites

The first satellite instrument which performed and still performs nadir PBL sensitive measurements of XCO₂ and XCH₄ in the relevant spectral regions in the short-wave infrared (SWIR) and near-infrared (NIR) is SCIAMACHY on ENVISAT, launched in 2002 (Burrows et al., 1995; Bovensmann et al., 1999). XCH₄ is the dry air column-averaged mole fraction or mixing ratio of CH₄ (in ppb). Different groups have developed dedicated radiative transfer and CO₂ and CH₄ retrieval algorithms for SCIAMACHY and used them for the analysis of the SCIAMACHY spectral observations (Buchwitz et al., 2000a,b, 2005a,b, 2007; Frankenberg et al., 2005, 2008; Gloudemans et al., 2005; Houweling et al., 2005; Barkley et al., 2007; Bösch et al., 2006; Schneising et al., 2008, 2009). It has been shown that SCIAMACHY can detect CO₂ variations of a few ppm, e.g., the CO₂ annual increase of about 2 ppm/yr and the northern hemispheric CO₂ seasonal cycle (Buchwitz et al., 2007; Schneising et al., 2008). It has also been shown that SCIAMACHY can detect regionally elevated CO₂ over strong and extended anthropogenic source regions when averaging several years of data (Schneising et al., 2008). The retrieval algorithm development for SCIAMACHY XCO₂ is ongoing to further improve the accuracy of the XCO₂ data product (Buchwitz et al., 2009; Reuter et al., 2010). This is also valid for SCIAMACHY XCH₄ (Frankenberg et al., 2008; Schneising et al., 2009) which has already been used to better constrain regional CH₄ emissions via inverse modeling (Bergamaschi et al., 2007, 2009) and to improve the global modeling of methane emissions (Bloom et al., 2010).

The dedicated GHG satellite missions Orbiting Carbon Observatory (OCO) (Kuang et al., 2002; Crisp et al., 2004; Miller et al., 2007) and Greenhouse Gases Observing Satellite (GOSAT) (Hamazaki et al., 2004; Kuze et al., 2009) have been built to perform highly accurate and precise global PBL sensitive XCO₂ measurements (and XCH₄ for GOSAT). Both instruments have been designed to perform nadir mode observations (over land) and sun-glint mode observations (over ocean) of high resolution spectra in well-selected absorption bands in the SWIR and NIR spectral regions. The spectral regions covered are CO₂ absorption bands around 1.6 and 2.0 μm and the O₂-A absorption band at 0.76 μm (O₂ is included to provide additional information on clouds

and aerosols and on the average surface pressure within the satellite's footprint). In contrast to OCO, GOSAT also covers absorption bands of CH₄, which is the second most important anthropogenic greenhouse gas. In addition, GOSAT also covers a large part of the thermal infrared (TIR) spectral region. GOSAT has been successfully launched in January 2009. OCO unfortunately failed during its launch in February 2009 (Palmer and Rayner, 2009). Dedicated retrieval algorithms have been developed for OCO (Bösch et al., 2006; Connor et al., 2008; Butz et al., 2009) and GOSAT (Oshchepkov et al., 2008; Bril et al., 2009) and a number of studies have been performed in order to assess their potential to reduce uncertainties in our knowledge on CO₂ sources and sinks (Miller et al., 2007; Chevallier et al., 2007; Feng et al., 2009; Baker et al., 2010).

In addition to SCIAMACHY and GOSAT, there are other satellite instruments that measure tropospheric CO₂ in nadir mode, namely HIRS/TOVS (Chédin et al., 2002, 2003), AIRS (Engelen et al., 2004; Engelen and Stephens, 2004; Engelen and McNally, 2005; Chevallier et al., 2005; Aumann et al., 2005; Strow et al., 2006), IASI (Crevoisier et al., 2009a) and TES (Kulawik et al., 2010). These sensors perform measurements in the TIR part of the electromagnetic spectrum. Nadir TIR measurements have highest sensitivity in the middle and upper troposphere but typically only little sensitivity for the lowest atmospheric layers, where the regional GHG source/sink signals are largest. Their information content with respect to regional CO₂ and CH₄ sources and sinks is therefore limited and retrievals are typically restricted to the tropics because of the difficulty to separate CO₂ variations from temperature variations (Chédin et al., 2003; Engelen and Stephens, 2004; Engelen et al., 2004; Chevallier et al., 2005; Crevoisier et al., 2009a,b). Active laser based satellite systems are also under investigation (see, e.g., Amediek et al., 2009; Bréon and Ciais, 2010, and references given therein).

Another promising approach is to use the complementary solar (SWIR/NIR) and thermal infrared (TIR) satellite nadir observations in combination (Christi and Stephens, 2004; Burrows et al., 2004) but also to combine data from passive and active CO₂ and CH₄ instrumentation.

3 Atmospheric signature of power plant emission plumes

In order to simulate the CO₂ vertical column enhancement at and downwind of a CO₂ emitting PP, a quasi-stationary Gaussian plume model is used, which is described in Appendix A. Figure 1 shows a typical example of a simulated CO₂ plume at high spatial resolution (left) and at a spatial resolution of 2×2 km² corresponding to the resolution of the CarbonSat satellite instrument discussed in detail below. As can be seen, the assumed CO₂ emission of 13 MtCO₂/yr results in an enhancement of the CO₂ vertical column of about

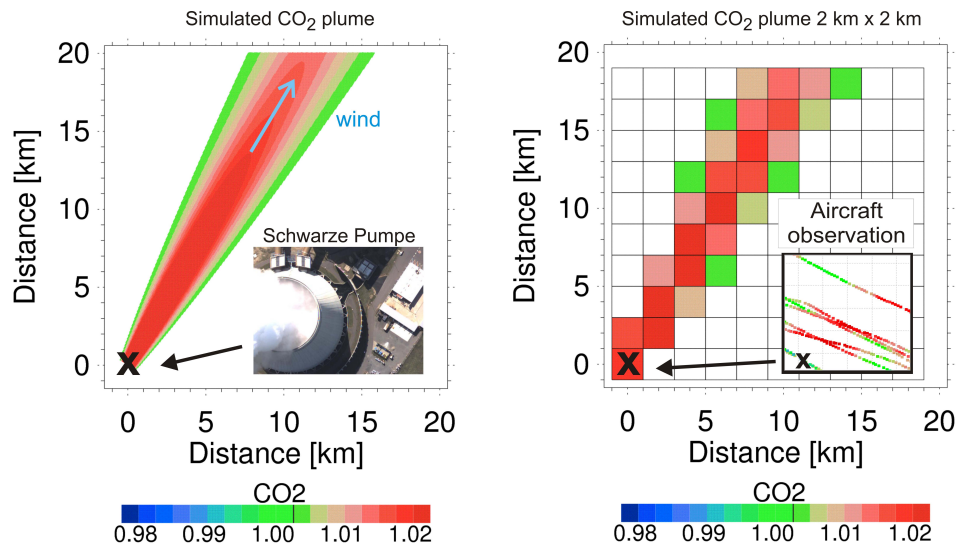


Fig. 1. Left: Simulation of the atmospheric CO₂ column enhancement due to CO₂ emission of a power plant using a quasi-stationary Gaussian plume model. The power plant location is indicated by the black cross. A value of 1.0 (green) corresponds to the background CO₂ column. A value of 1.02 (red) corresponds to a column enhancement of 2% or larger relative to the background. The wind speed is 1 m/s. The assumed power plant emission is 13 MtCO₂/yr corresponding to a power plant such as Schwarze Pumpe located in eastern Germany near Berlin (see photo taken during an overflight with the MAMAP aircraft instrument). Right: as left hand side but at a spatial resolution of 2×2 km² obtained by box-car averaging the high resolution plume shown on the left hand side. The inset shows MAMAP CO₂ column retrievals around the location of the power plant Schwarze Pumpe (see main text and Fig. 2 for details). The maximum value of the CO₂ normalized column is 1.126 for the high resolution plume on the left (resolution 20×20 m²) and 1.031 for the 2×2 km² resolution plume shown on the right. To better visualize the extent of the CO₂ plumes values below 1.0025 are shown in white (see also the black vertical line in the color bar).

Table 1. Maximum CO₂ column enhancement (relative to background column (=1.0)) for a power plant emitting 13 MtCO₂/yr for different spatial resolutions of the satellite footprint. The assumed wind speed is 1 m/s.

Horizontal resolution	Peak of CO ₂ column normalized to background (-)	Comment
20 m×20 m	1.126	see Fig. 1 left
40 m×40 m	1.125	
1 km×1 km	1.053	
2 km×2 km	1.031	see Fig. 1 right
4 km×4 km	1.017	
10 km×10 km	1.005	

2% at a spatial resolution of 2×2 km² (the maximum value is 3.1% as shown in Table 1). If the ground pixel size is 10 km, which corresponds to the ground pixel size of GOSAT, the CO₂ emission only results in a CO₂ column enhancement of 0.5% of the background column (see Table 1). High spatial resolution imaging is therefore important for this application.

Also shown in Fig. 1 are aircraft CO₂ column retrievals performed using the Methane Airborne Mapper (MAMAP) aircraft instrument (Gerilowski et al., 2010). The MAMAP CO₂ observations agree reasonably well with the Gaussian

plume model simulation. MAMAP is a spectrometer system primarily developed for measuring CH₄ vertical columns or sub-columns from aircraft but covers also CO₂ absorption bands around 1.6 μm. MAMAP has been jointly developed by GFZ-Potsdam and IUP-Bremen. MAMAP covers similar spectral regions as CarbonSat (see Sect. 5.1) and is therefore used as an airborne demonstrator for the CarbonSat concept.

The MAMAP results displayed in Fig. 1 are shown in more detail in Fig. 2. They are based on CO₂ and CH₄ column retrievals applied to data obtained during a flight with the Cessna aircraft of the Free University of Berlin (FU Berlin) over the lignite burning power plant Schwarze Pumpe located in eastern Germany near Berlin (latitude 51.54° N, longitude 14.35° E). For the time of the overflight on 26 July 2007 the CO₂ emission of Schwarze Pumpe is reported to be 13 MtCO₂/yr (Dietmar Heinze, Vattenfall Europe Generation AG & Co. KG, Cottbus, Germany, personal communication, 2008). The normalized CO₂ columns shown in Fig. 2a have been obtained by normalizing the retrieved CO₂ columns by simultaneously retrieved CH₄ columns from the same spectrometer band (“CH₄ proxy” approach). Note that the scale used for the aircraft observations is ±3% compared to ±2% for the plume simulation. The reason for this is that the altitude sensitivity of MAMAP, characterized by the MAMAP averaging kernels, has not been considered for the results

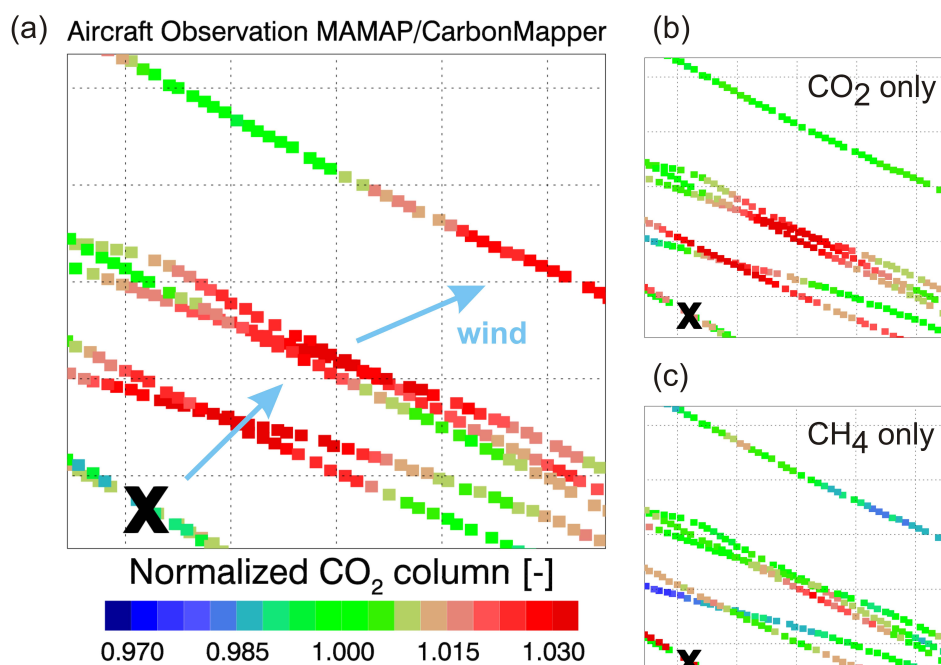


Fig. 2. (a) Normalized CO₂ columns as retrieved from MAMAP aircraft observations on 26 July 2007. The CO₂ columns have been normalized by simultaneously retrieved CH₄ columns. (b) Retrieved CO₂ columns without normalization by CH₄. (c) Retrieved CH₄ columns. The black cross indicates the location of the power plant Schwarze Pumpe (latitude 51.54° N, longitude 14.35° E), Germany. The blue arrows indicate the approximate wind direction, which changed during the time of the measurements.

shown here. Figure 2b shows normalized CO₂ columns obtained by normalizing the retrieved CO₂ column by its own average (i.e., not by CH₄).

As can be seen, the CO₂ column enhancement due to the CO₂ emission of the PP is also clearly visible in Fig. 2b. The CO₂ columns shown in Fig. 2b suffer to some extent from light path related errors due to, e.g., aircraft movements not yet considered in the retrieval and scattering related effects caused by the variability of aerosols and clouds, which are also not yet considered in the retrieval. Figure 2c shows the normalized CH₄ columns obtained by normalizing the retrieved CH₄ column by its own scene average, as also done for the CO₂ shown in Fig. 2b. Although the retrieved CH₄ shows significant variability, the pattern is significantly different from the CO₂ pattern. No clear correlation with the PP location and the wind direction is visible. Assuming constant atmospheric CH₄ and noise free observations, the pattern of the retrieved CH₄ would show the light path error. As the CO₂ and CH₄ columns are retrieved using the same preliminary version of the retrieval algorithm, the columns of both retrieved gases suffer from nearly identical light path errors. Assuming constant atmospheric CH₄ over the scene of interest allows to eliminate the light path error to a large extent by normalizing the retrieved CO₂ column with the retrieved CH₄ column as done for the normalized CO₂ columns shown in Fig. 2a.

The MAMAP flight data are currently being analyzed to quantitatively determine the CO₂ emission and its associated uncertainty of the Schwarze Pumpe power plant from the MAMAP spectral observations (Krings et al., 2010).

These results indicate that a satellite which aims at detection and monitoring of PP CO₂ emissions needs to have high spatial resolution, e.g., a ground pixel size of about 2 km or smaller. This is necessary in order to detect the CO₂ emission plume but also to increase the probability for sufficiently cloud free scenes. The results also indicate that the single ground pixel CO₂ column retrieval precision needs to be better than 1% as this is the expected order of the CO₂ column enhancement relative to the background. In addition, a number of other criteria need to be fulfilled. For example the satellite's swath width needs to be sufficiently large to achieve frequent mapping of PPs and their surroundings.

In the next section a mission concept for a single satellite is presented which has the potential to fulfill the requirements for PP CO₂ emission monitoring in addition to the requirements that need to be fulfilled for global regional-scale CO₂ and CH₄ surface flux inverse modeling as have been identified in or can be derived from various studies (Crisp et al., 2004; Houweling et al., 2004; Meirink et al., 2006, 2008; Miller et al., 2007; Chevallier et al., 2007; Bergamaschi et al., 2009; Feng et al., 2009; Baker et al., 2010).

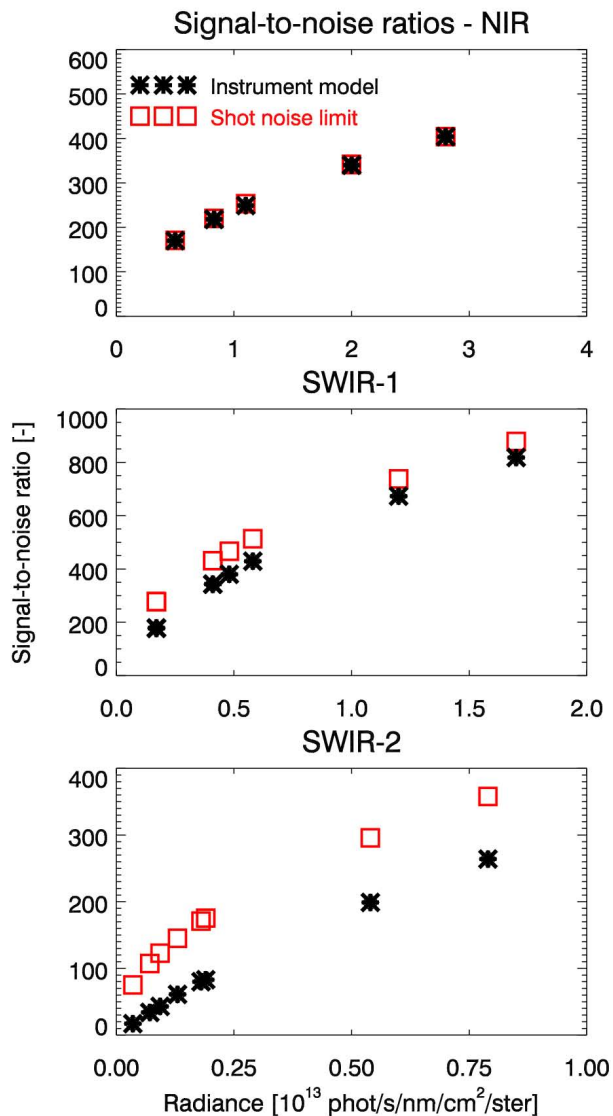


Fig. 3. Signal-to-noise ratios (SNRs) as a function of the radiance as measured by CarbonSat in nadir mode for the eight scenarios listed in Table 3. The black crosses show the SNRs computed using the instrument model described in Sect. 5.1. The red squares show the SNRs which can be obtained in the shot noise limit ($\text{SNR}=\sqrt{S}$).

4 CarbonSat mission concept

In order to achieve frequent PP overpasses and global coverage within a few days with a single satellite, a low Earth orbiting (LEO) satellite mission with a sufficiently large swath width is needed. As the satellite shall measure reflected solar radiation to be sensitive to near-surface CO₂ concentration changes, the solar zenith angle (SZA) needs to be as small as possible. For a sun-synchronous orbit an equator local overpass time around noon would be ideal. However other aspects such as minimum cloud cover also need to be considered. In addition, it would be advantageous to use as

much as possible available relevant information from other satellites. Most important in this context is additional cloud and aerosol information, in particular sub-scene (sub ground pixel) information. In this context a good co-location with NOAA/NASA's "Joint Polar Satellite System" (JPSS) meteorological afternoon satellite ("NPOESS C1") would be a goal opportunity, primarily in order to use the relatively high spatial resolution cloud and aerosol information from the VIIRS instrument (see, e.g., <http://www.npoess.noaa.gov/>). In the following it is therefore assumed that the CarbonSat orbit is similar to the NPOESS C1 orbit (Local Time Ascending Node (LTAN) 13:30 LT, repeat track 17 days), which is similar to the orbit which had been chosen for OCO.

For the purpose of this study the scientific payload of CarbonSat is assumed to consist of a single instrument, the CarbonSat Imaging Spectrometer (IS). It is however planned to equip CarbonSat also with a Cloud and Aerosol Imager (CAI) similar to the CAI onboard GOSAT (Kuze et al., 2009). The CarbonSat-IS instrument shall be designed to measure dry air column-averaged mixing ratios of CO₂ and CH₄. The measurement precision and coverage shall be high enough to not only detect and quantify PP CO₂ emissions but also to allow the quantification of CO₂ and CH₄ surface fluxes at weekly or monthly time resolution at a spatial resolution of about 500×500 km² globally (with some gaps, e.g., around the poles). The mission objectives are therefore similar to the mission objectives of OCO (Crisp et al., 2004) and GOSAT (Hamazaki et al., 2004; Kuze et al., 2009). Compared to OCO and GOSAT, CarbonSat will however have important additional capabilities such as better spatial sampling and coverage due to CarbonSat's wide swath imaging capability. Compared to OCO, CarbonSat will have a much wider swath (500 km compared to 10 km for OCO) and will also enable the retrieval of methane. This is achieved by including the relevant spectral region in the SWIR (1.65 μm) covered by methane absorption lines. In contrast to GOSAT, which has a ground pixel size of 10 km with gaps of about 150 km between the individual ground pixels, CarbonSat shall have a ground pixel size of 2 km and no gaps between the ground pixels (across track and along track). This allows the generation of CO₂ and CH₄ maps without gaps as needed for the unambiguous detection and frequent coverage of power plants and other strong emission targets. This will also help to get more accurate regional scale CO₂ and CH₄ surface fluxes because dense sampling poses less stringent requirements on the modeling of the atmospheric transport.

The global regional-scale CO₂ surface flux inverse modeling application implies demanding requirements, e.g., in terms of precision and accuracy (Houweling et al., 2004; Miller et al., 2007; Chevallier et al., 2007). For CH₄ the requirements are also high but somewhat less demanding (Meirink et al., 2006; Bergamaschi et al., 2007, 2009). These challenging requirements are considered for the instrument concept as described in the following. They are however not discussed in detail as this is not the focus of this study.

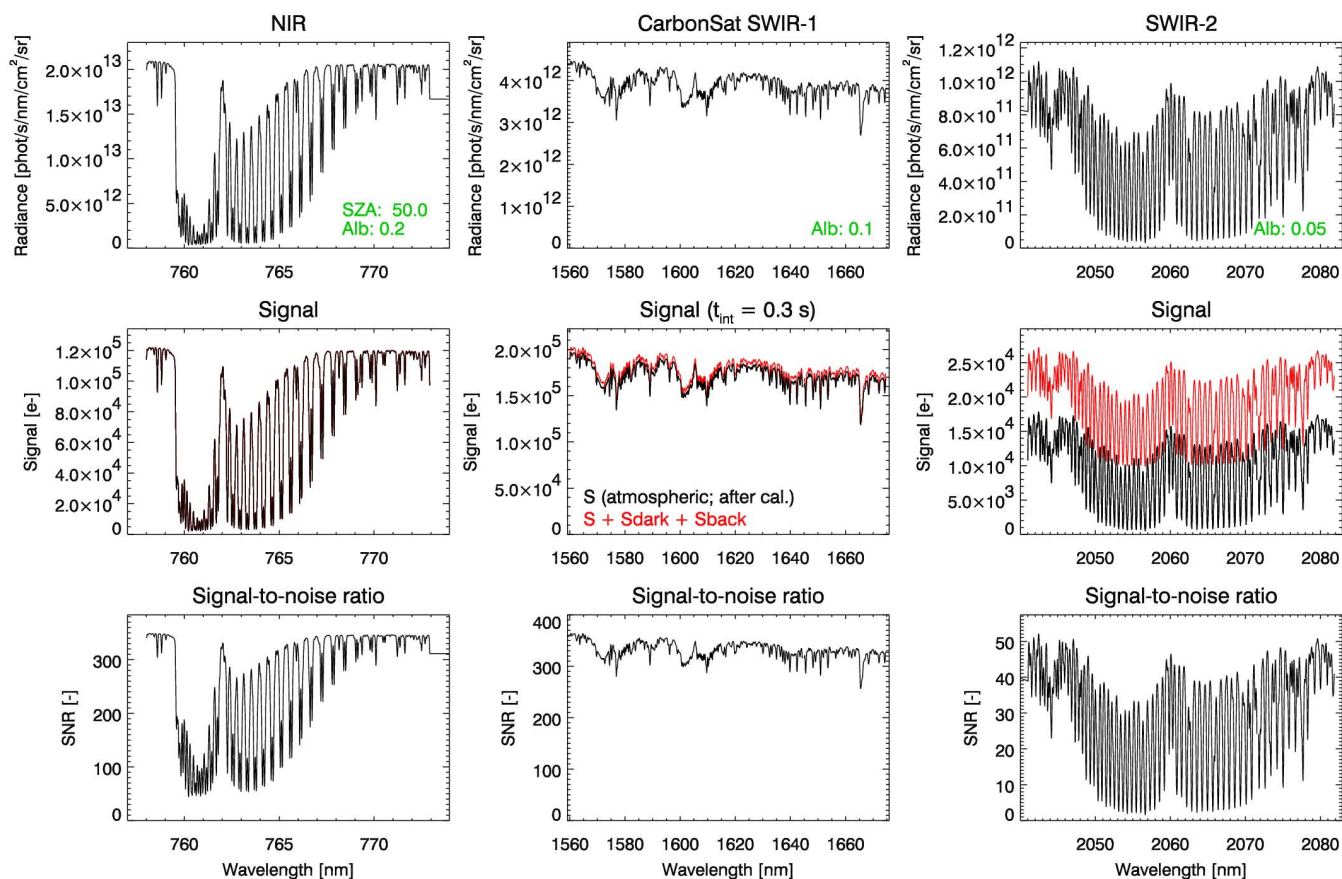


Fig. 4. Results of the CarbonSat instrument simulation for the VEG₅₀ scenario (albedo: vegetation, SZA 50°) for an integration time of $t_{\text{int}} = 0.3$ s. Top: Radiance spectra in the three spectral bands covered by CarbonSat. Middle: corresponding signal (in electrons; red: before calibration; black: after calibration, i.e., after subtraction of detector dark and thermal background radiation signals). Bottom: corresponding signal-to-noise ratio.

Figure 4 shows simulated CarbonSat sun-normalized radiance spectra (top row panels). The middle panel shows the relatively transparent spectral region around 1.6 μm which will deliver the main information about the CO₂ and CH₄ columns (“SWIR-1 band”). The O₂-A-band spectral region is included to provide additional information on clouds, aerosols, and surface pressure (“NIR band”). The right panel shows the spectral region where CO₂ has very strong absorption lines (“SWIR-2 band”). This band will mainly be used to further reduce CO₂ retrieval errors caused by clouds and aerosols. The spectral regions covered by CarbonSat are similar to the spectral regions covered by OCO except that an extended region around 1.6 μm is used to also measure methane. The spectrometer system is described in more detail in the next section.

5 Observing System Simulation Experiments (OSSE)

In order to estimate random and systematic errors of the PP CO₂ emissions to be derived from CarbonSat observations, Observing System Simulation Experiments (OSSE) have been conducted.

Each OSSE consists of a number of different simulation steps which are described in the following sub-sections starting with the instrument simulation.

5.1 Instrument model

In this section a technically feasible instrument concept is described and it is explained how signal-to-noise ratios (SNRs) of the radiance spectra have been computed. The signal-to-noise ratio determines the theoretically achievable X_{CO_2} retrieval precision and therefore also determines the single overpass PP CO₂ emission detection limit.

Detailed instrument parameters needed for the SNR computations are specified primarily to demonstrate that the required instrument performance can be achieved with realistic

Table 2. CarbonSat’s spectral bands, assumed performance parameters and corresponding signal-to-noise ratios (SNRs). Each band is assumed to be equipped with a Focal Plane Array (FPA) with 1000×250 detector pixels in the spectral and spatial directions, respectively. The spectral resolution is specified in terms of the Full Width at Half Maximum (FWHM) of the spectrometer’s line shape function. The spectral sampling ratio, N_{sr} , is the number of detector pixels per FWHM. The SNR refers to the continuum SNR outside strong absorption lines for nadir measurements with an integration time of $t_{int}=0.3$ s and for a ground pixel size of 4 km². The assumed orbit altitude is 800 km. The SNRs are given for 8 scenarios which differ by surface albedo and solar zenith angle (SZA) (see also Table 3).

Parameter	Band		
	NIR	SWIR-1	SWIR-2
Spectral range (nm)	757–775	1559–1675	2043–2095
Spectral resolution FWHM (nm)	0.045	0.34	0.123
Spectral sampling ratio N_{sr}	3	3	3
Transmission τ (–)	0.5	0.5	0.5
Quantum efficiency QE (electrons/photon)	0.6	0.6	0.6
Detector area A_{det} (10 ^{–6} cm ²)	5.76	5.76	5.76
F -number F_{num} (–)	2.0	2.0	2.0
Detector dark current I_{dark} (fA)	0.1	3.0	3.0
Thermal background current I_{back} (fA)	0.0	0.0	2.0
Readout noise N_{read} (electrons r.m.s.)	6	300	300
Continuum SNR (–):			
VEG_25: Vegetation, SZA=25°	410	420	70
SAS_25: Sand/soil, SZA=25°	410	800	290
VEG_50: Vegetation, SZA=50°	340	340	50
SAS_50: Sand/soil, SZA=50°	330	620	220
A01_50: Albedo=0.1, SZA=50°	250	350	90
A005_60: Albedo=0.05, SZA=60°	170	180	40
VEG_75: Vegetation, SZA=75°	220	180	22
SAS_75: Sand/soil, SZA=75°	220	380	100

instrument parameters in line with current technology. Reasonable values for all parameters have been selected. They do not necessarily reflect the latest results from the (ongoing) specification of CarbonSat.

The instrument is assumed to be an imaging grating spectrometer system which covers the three spectral bands introduced above. Each band is covered by a Focal Plane Array (FPA) which is assumed to consist of at least 1000 spectral detector pixels times at least 250 detector pixels in the spatial (across track) direction.

The SNR of the three bands determines to a large degree if the PP emission signals can be detected. To estimate the SNR using radiance spectra and given instrument parameters a simple but realistic instrument model is used. The SNR is defined as follows:

$$SNR = \frac{S}{N}, \quad (1)$$

where S is the measured signal (in electrons). S is the “atmospheric” signal after calibration, i.e., after subtraction of the signal generated by the instrument. N is the noise (in electrons root mean square (r.m.s.)). The signal S is computed as follows:

$$S = R \times \tau \times QE \times A_{det}/F_{num}^2 \times N_{sr} \times \Delta\lambda \times t_{int}, \quad (2)$$

where R is the observed radiance (in photons/s/nm/cm²/steradian), τ is the dimensionless throughput or transmission of a channel, and QE is the detector quantum efficiency. $\Delta\lambda$ is the detector pixel’s spectral bandwidth (in nanometer), which is equal to the spectral resolution Full Width at Half Maximum (FWHM) of the instrument line shape function divided by the spectral sampling ratio N_{sr} , i.e., the number of detector pixels per FWHM. A_{det} is the detector pixel area, F_{num} is the F -number of the spectrometer, and t_{int} is the integration or exposure time.

Note that the term $A_{det}/F_{num}^2 \times N_{sr}$ is equal to $A_{ap} \times \Omega/N_{sr}$, where A_{ap} is the spectrometer aperture area and Ω is the spectrometer acceptance (solid) angle. The product $A_{ap} \times \Omega$ is typically referred to as etendue. Ω is determined by the ground pixel size and the orbit altitude. A_{ap} needs to be chosen sufficiently large to ensure an appropriate instrument performance, e.g., in terms of the required signal to noise ratio. Alternatively, the instrument can be specified by its F -number, F_{num} , which needs to be chosen sufficiently small to get the desired performance.

The noise N consists of four terms, the atmospheric signal shot noise term (\sqrt{S}), the detector dark signal shot noise term ($\sqrt{S_{dark}}$), the thermal background radiation signal shot noise

term ($\sqrt{S_{\text{back}}}$) and the electronic readout noise term N_{read} :

$$N = \sqrt{S + S_{\text{dark}} + S_{\text{back}} + N_{\text{read}}^2} \quad (3)$$

The dark signal S_{dark} (in electrons) is computed as follows:

$$S_{\text{dark}} = I_{\text{dark}} \times t_{\text{int}} \times Q, \quad (4)$$

where I_{dark} is the dark current in Ampere and Q equals 6.242×10^{18} electrons/Coulomb. The signal caused by the thermal background radiation of the instrument, S_{back} (in electrons), is given by:

$$S_{\text{back}} = I_{\text{back}} \times t_{\text{int}} \times Q, \quad (5)$$

where I_{back} is the background signal in Ampere. Realistic numerical values of these parameters are listed in Table 2 along with the resulting SNR for 8 scenarios. It is not the intention of this study to investigate in detail the performance of specific existing devices. Instead typical performance parameters are used. Several manufacturers offer NIR and SWIR FPA's with (at least) 1024 times 256 detector pixels, which are appropriate for the application investigated here. The sizes of the individual detector pixels are similar to the size used here ($24 \mu\text{m} \times 24 \mu\text{m}$). The values used here for the readout noise are on the order of the values given by different manufacturers. This is also true for the assumed quantum efficiency. The dark current significantly depends on the operating temperature of the detector. It is assumed here that a temperature low enough is used to ensure sufficiently low dark signal (the default value assumed here is 3 fA for the SWIR bands). The thermal background signal depends on the temperature of the optical bench. It is assumed that the optical bench temperature will be low enough to achieve a good performance (the default value used here is 2 fA for the SWIR-2 band). The values assumed here for the optical throughput τ are also realistic (V. Mogulsky, Kayser-Threde GmbH, Munich, Germany, personal communication). The F -number is chosen to be 2, which is close to the F -number of OCO (1.8).

Eight observation scenarios have been defined for the simulation of nadir measurements over land. They differ in surface albedo and solar zenith angle (SZA) as can be seen from Table 2. These are the two most important parameters which determine the radiance level and therefore the SNR. An overview about the scenarios is given in Table 3. Different wavelength dependent surface albedos have been defined for the scenarios corresponding to vegetation ("VEG" scenarios) and sand/soil ("SAS" scenarios) land surfaces. In addition, scenarios with a constant surface albedo have been defined. The same aerosol scenario has been used for all 8 scenarios (see caption Table 3).

In Bösch et al. (2006), SNR values for OCO are listed for a scenario with an albedo of 0.05 and a solar zenith angle of 60° which can be compared with the SNRs listed in Table 2 for the A005_60 scenario. For the O₂-A-band (NIR band) the reported SNR for OCO is 360 (here: 170), for the weak CO₂

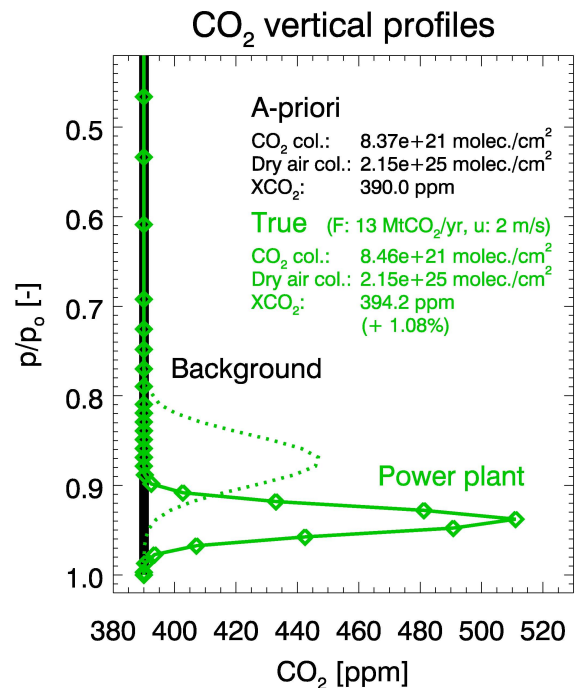


Fig. 5. A-priori (black) and perturbed (green) CO₂ mixing ratio vertical profiles used for the simulated CarbonSat measurements. The solid green line corresponds to the CO₂ mixing ratio profile at a distance of 1.41 km from the power plant (as shown by the annotation the XCO₂ is enhanced by 1.08% relative to the background XCO₂, which is 390.0 ppm), the dotted green profile corresponds to a distance of 2.24 km from the power plant. The assumed power plant emission is $F=13 \text{ MtCO}_2/\text{yr}$ and the assumed wind speed is $u=2 \text{ m/s}$.

band (SWIR-1) the OCO SNR is 250 (here: 180), and for the strong CO₂ band (SWIR-2) the OCO SNR is 180 (here: 40). The SNRs for OCO are higher than those for CarbonSat, as significant binning (co-adding) of spectra is applied. This is possible for OCO due to its small number of across-track ground pixel compared to CarbonSat (OCO: 8 across-track ground pixel and 10 km swath width, CarbonSat: 250 ground pixel and 500 km swath width).

Note that the SNRs listed in Table 2 differ somewhat compared to the SNRs given in Table 2 of Bovensmann et al. (2010), as the updated simulations differ slightly with respect to integration time and aerosol scenario (see above). Figure 3 shows the SNR as a function of the radiance measured in nadir mode. The SNR has been computed using the approach and parameters presented above. Also shown in Fig. 3 is the SNR in the shot noise limit, i.e., assuming no noise contributions from the detector and its readout electronics and from the thermal background radiation. The optimization of the CarbonSat instrument concept is an ongoing activity but for the results presented in this publication the instrument parameters have not been updated, i.e., are identical with the ones used in the AMTD version of

Table 3. Specification of eight scenarios and corresponding retrieval precisions for CO₂ and CH₄ columns, surface pressure (p_o), $XCO_2(p_o)$ and $XCO_2(CH_4)$ for CarbonSat nadir mode observations. $XCO_2(p_o)$ refers to XCO_2 obtained using the “ p_o -proxy method” and $XCO_2(CH_4)$ refers to XCO_2 obtained using the “CH₄-proxy method” (see main text for details). Aerosol scenario: single scattering albedo 0.999, Henyey-Greenstein phase function with asymmetry parameter 0.7, aerosol optical depth (AOD) 0.2 at 550 nm with λ^{-1} wavelength dependence.

Scenario		Surface albedo (–) NIR / SWIR-1 / SWIR-2	SZA (deg.)	CO ₂ col. (%)	p_o (%)	Retrieval precision		
						CH ₄ col. (%)	$XCO_2(p_o)$ (ppm)	$XCO_2(CH_4)$ (ppm)
VEG_25:	Vegetation, SZA=25°	0.20/0.10/0.05	25	0.26	0.08	0.37	1.1	1.8
SAS_25:	Sand/soil, SZA=25°	0.20/0.30/0.30	25	0.14	0.07	0.21	0.6	0.9
VEG_50:	Vegetation, SZA=50°	0.20/0.10/0.05	50	0.29	0.06	0.42	1.2	2.0
SAS_50:	Sand/soil, SZA=50°	0.20/0.30/0.30	50	0.17	0.06	0.23	0.7	1.1
A01_50:	Albedo=0.1, SZA=50°	0.10/0.10/0.10	50	0.27	0.07	0.42	1.1	1.9
A005_60:	Albedo=0.05, SZA=60°	0.05/0.05/0.05	60	0.43	0.14	0.77	1.8	3.4
VEG_75:	Vegetation, SZA=75°	0.20/0.10/0.05	75	0.40	0.11	0.63	1.6	2.9
SAS_75:	Sand/soil, SZA=75°	0.20/0.30/0.30	75	0.24	0.11	0.31	1.0	1.5

this manuscript (Bovensmann et al., 2010). As indicated by Fig. 3, the SNR of the SWIR-2 band can be improved by minimising the noise due to thermal background radiation. Ongoing activities indicate that for SWIR-2 a significantly higher SNR is achievable. Therefore, depending on detector choice and instrument temperature, significant improvements in the SNR performance especially for the SWIR-2 band can be expected. The SNR values used in this study are therefore conservative estimates, especially for the SWIR-2 band.

The signal and the SNR for the vegetation scenario with a SZA of 50° are shown in Fig. 4. The SNR is important as it determines the theoretically achievable retrieval precision of the atmospheric parameters. How the CO₂ retrieval precision is obtained from the simulated signal and its error (inverse SNR) is described in the next section.

5.2 Atmospheric CO₂ retrievals

In order to estimate the CO₂ column retrieval precision given the measured spectrum and its error an Optimal Estimation (OE) retrieval algorithm is used. The underlying theory is described in detail in (Rodgers, 2000). The algorithm used is an initial implementation of a new algorithm which is under development for improved SCIAMACHY CO₂ retrieval, and is referred to as “Bremen optimal ESTimation DOAS” (BESD) (Buchwitz et al., 2009; Reuter et al., 2010). The version of BESD used here for CarbonSat significantly differs from the versions used for SCIAMACHY described in Buchwitz et al. (2009) and Reuter et al. (2010), e.g., with respect to the state vector elements. Below we give a short description of BESD as used for this study. A detailed description is given in Appendix B.

CarbonSat is assumed to measure radiance spectra $R_i \equiv R(\lambda_i)$ in nadir mode at discrete wavelengths λ_i as well as the solar irradiance, $F_i \equiv F(\lambda_i)$. From these two quantities the (measured) sun-normalized radiance or intensity I_i can

be computed: $I_i \equiv \pi R_i / F_i$. Measurement vector \mathbf{y} has elements $y_i \equiv \ln(I_i)$. The corresponding model quantity \mathbf{y}^{mod} is obtained with the radiative transfer model (RTM) SCIA-TRAN (Buchwitz et al., 2000a; Rozanov et al., 2002). The version of BESD used for this study is based on linearizing the logarithm of the sun-normalized radiance around an assumed (atmospheric) state denoted by the a priori state vector \mathbf{x}_a , i.e., the following equation is used for \mathbf{y}^{mod} as a function of state vector \mathbf{x} :

$$\mathbf{y}^{\text{mod}}(\mathbf{x}) = \mathbf{y}_a + \mathbf{K}(\mathbf{x} - \mathbf{x}_a). \quad (6)$$

Here $\mathbf{y}_a \equiv \mathbf{y}^{\text{mod}}(\mathbf{x}_a)$, i.e., \mathbf{y}_a is the logarithm of the intensity for state vector \mathbf{x}_a . Matrix \mathbf{K} contains the derivatives of the logarithm of the intensity with respect to the state vector elements and is typically referred to as Jacobian matrix.

BESD is based on minimizing the following cost function $C(\mathbf{x})$:

$$C(\mathbf{x}) = (\mathbf{x} - \mathbf{x}_a)^T \mathbf{S}_{x_a}^{-1} (\mathbf{x} - \mathbf{x}_a) + (\mathbf{y} - \mathbf{y}^{\text{mod}}(\mathbf{x}))^T \mathbf{S}_y^{-1} (\mathbf{y} - \mathbf{y}^{\text{mod}}(\mathbf{x})). \quad (7)$$

Here \mathbf{S}_{x_a} is the a-priori uncertainty (or variance/covariance) matrix of state vector \mathbf{x}_a . \mathbf{S}_y is the measurement error variance/covariance matrix. $()^T$ denotes matrix transpose and $()^{-1}$ denotes matrix inverse. The solution of this estimation problem is an estimate of the state vector, $\hat{\mathbf{x}}$, and its variance/covariance matrix $\hat{\mathbf{S}}_{\hat{\mathbf{x}}}$ (how this solution can be obtained is described in Appendix B).

The simulated CarbonSat radiance measurements have been obtained by solving the full multiple scattering radiative transfer equation without assuming linearity. For the simulations different CO₂ mixing ratio profiles have been defined. The a-priori CO₂ profile has a constant mixing ratio of 390 ppm. For the simulated measurements at and around PPs the CO₂ profiles with enhanced mixing ratios in the lowest 1–2 km of the atmosphere have been defined. This enhancement is assumed to be caused by the PP CO₂ emission. The a-priori profile and two profiles at two different distances

from the location of the PP are shown in Fig. 5 along with the numerical values of the corresponding CO₂ vertical columns and XCO₂. As can be seen, the profiles have been defined such that the peak altitude of the CO₂ mixing ratio and the vertical width increase with increasing distance from the PP.

Of concern are of course not only random errors but also systematic errors especially due to clouds and aerosols. It is assumed that only sufficiently cloud free scenes are useful for the application discussed here. Furthermore, the BESD retrieval algorithm accounts to some extent for disturbing scattering effects due to residual (i.e., very thin and/or very small, i.e., sub-pixel) clouds and aerosols. This is achieved by exploiting the information content of the three spectral regions, in particular the two spectral regions covered by the NIR and the SWIR-2 bands (Kuang et al., 2002). Additional very useful information can be obtained from the simultaneously retrieved methane column using its absorption lines located next to the CO₂ lines in band SWIR-1 as the retrieved methane column will suffer from similar scattering related errors as the retrieved CO₂ column. This can be used to identify and correct scattering related biases similar to what is done for SCIAMACHY methane retrieval (Frankenberg et al., 2005, 2008; Schneising et al., 2009). This approach requires that the methane variability is small compared to the variability of CO₂ over the scene of interest (in terms of the relative enhancement of the vertical column) as is typically the case for the application discussed here.

Table 3 lists XCO₂ retrieval precisions obtained using two different methods: (i) using the retrieved surface pressure (p_o ; this information comes primarily from the O₂-A-band spectral region, see Jacobian for state vector element PSU_00 in Appendix 2 Fig. B1); this method is referred to as “ p_o -proxy method” in this manuscript and the corresponding XCO₂ is denoted XCO₂(p_o), and (ii) the “CH₄-proxy method”, based on the simultaneously retrieved CH₄ column used to convert the retrieved CO₂ column into a dry air column-averaged mixing ratio referred to as XCO₂(CH₄) in this manuscript (the exact definition is given in Appendix B). As can be seen from Table 3, the statistical uncertainty of the retrieved XCO₂(p_o) is better (smaller) compared to XCO₂(CH₄). The main reason for this is the higher SNR in the NIR band (O₂-A-band) compared to the SWIR-1 band where the CH₄ column information is coming from. As can be seen, the XCO₂(p_o) retrieval precision is typically in the 1–2 ppm range (0.25–0.5%) for all cases. The XCO₂(CH₄) retrieval precision is 2 ppm (0.5%) or better for the vegetation and soil albedo scenarios except for the (low albedo and low sun) VEG_75 scenario.

A statistical error of the retrieved atmospheric CO₂ due to instrument noise as discussed in this section results in uncertainties of the inferred PP CO₂ emission. How these emission uncertainties can be estimated is described in the next section, where also other error sources are discussed, including systematic errors.

5.3 Error analysis

In this section uncertainties of the retrieved PP CO₂ emissions are quantified. For this purpose the quasi stationary Gaussian plume forward model introduced in Sect. 3 is used in combination with a weighted linear least-squares emission flux inversion method. The impact of random and systematic errors of the CarbonSat XCO₂ (or CO₂ column) observations at and around the location of the PPs on the inferred emission is quantified for different conditions and error sources.

The model used to fit the simulated plume to the XCO₂ observations has two free parameters: (i) the PP CO₂ emission, F , and (ii) a background atmospheric CO₂ scaling parameter, denoted s , which has been added to the model to ensure that the emission flux inversion is less sensitive to systematic errors of the background XCO₂. The scaling factor, s , ensures that the flux inversion is insensitive to a constant (scene independent) multiplicative XCO₂ retrieval error. These type of errors may result from erroneous assumptions on the background aerosol, the assumed methane a-priori profile (if the “CH₄-proxy method” is used to obtain XCO₂), errors of spectroscopic parameters (e.g., line strength), or other reasons. Including the scaling parameters in the least-squares fit ensures that only the “differential” CO₂ column enhancement due to the PP CO₂ emission relative to the background is exploited in order to infer the PP CO₂ emission from the observed atmospheric CO₂ spatial pattern.

The theoretical retrieval precision is an important quantity to characterize the performance of the satellite as it essentially determines the detection limit of the sensor. Of course of concern are also other errors caused by, e.g., unaccounted or not perfectly accounted scattering effects by aerosols and clouds and errors resulting from imperfect knowledge of critical meteorological parameters such as wind speed, wind direction and horizontal mixing. In the following, initial error estimates for these (typically systematic) error sources are also presented and discussed. A full discussion of (all) systematic errors is out of the scope of this study.

End-to-end OSSE have been performed in order to estimate random and important systematic errors (aerosols, vertical CO₂ and CH₄ profiles, clouds, atmospheric transport) of the inferred PP emissions based on the satellite CO₂ observations and their random and systematic errors. In the following section, this is illustrated using radiance and SNR simulations for the VEG_50 scenario and for aerosol related systematic XCO₂ retrieval errors.

5.3.1 Errors due to aerosols

Figure 6 shows OSSE results for a scenario defined to quantify aerosol related errors. The simulation is valid for a surface albedo corresponding to vegetation and for a SZA of 50°, i.e., for the VEG_50 scenario. The assumed true PP emission is $F_{\text{true}} = 13.0 \text{ MtCO}_2/\text{yr}$ the assumed wind speed is $u = 2 \text{ m/s}$ (see annotation in the top right of Fig. 6). Shown

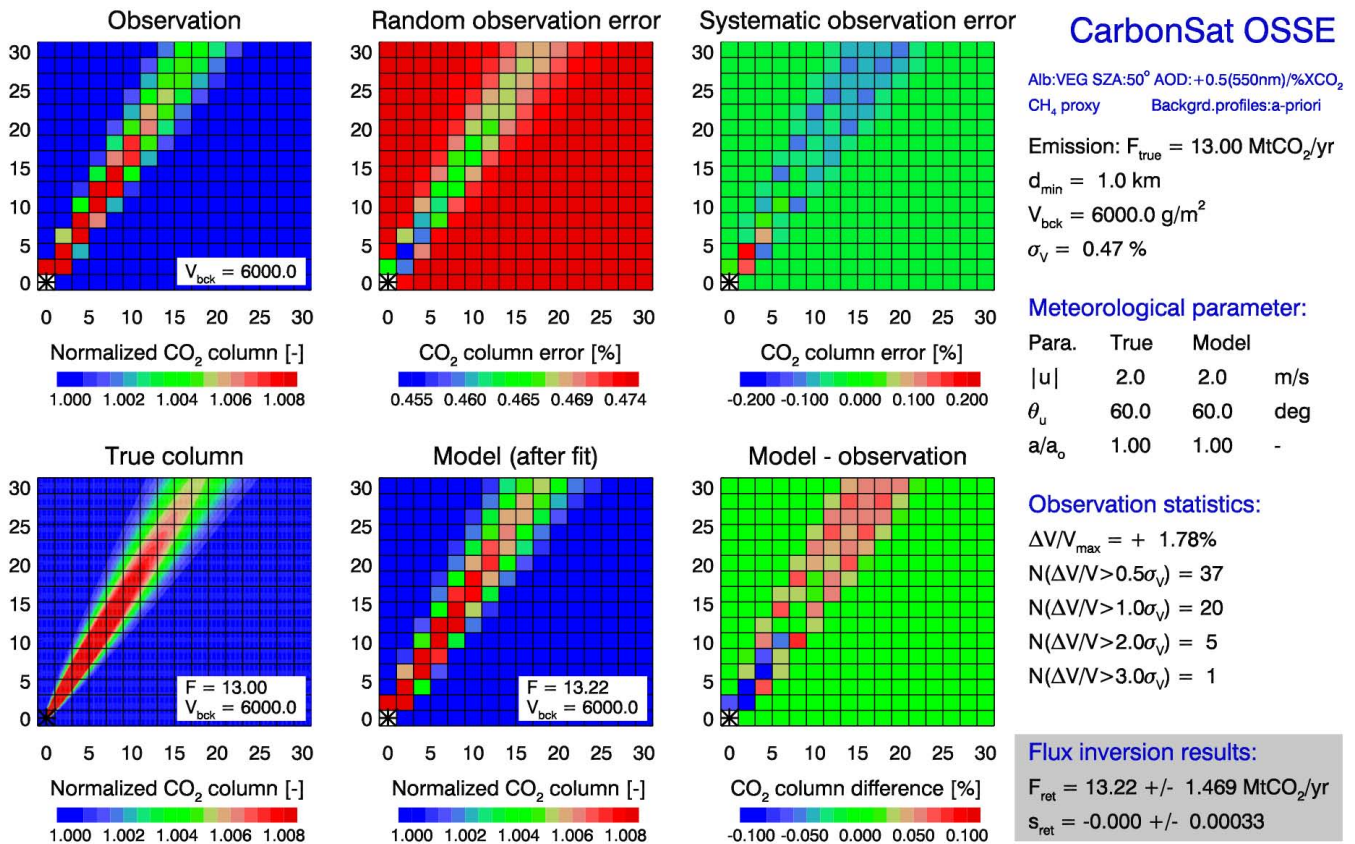


Fig. 6. Detailed results from a CarbonSat Observing System Simulation Experiment (OSSE) conducted to quantify random and systematic errors of power plant (PP) CO₂ emissions. Starting point is the simulation of the true CO₂ emission plume of a PP shown in the bottom left panel (“True column”). The PP is located in the bottom left corner of each panel. The assumed true emission is $F=13.0 \text{ MtCO}_2/\text{yr}$. Shown is the horizontal distribution of the normalized CO₂ column (normalized to the background column of 6000 g/m^2) or, equivalently, normalized XCO₂. The top row panels show (from left to right) the CO₂ columns as observed by CarbonSat and their random and systematic errors. The random error (1-sigma) originates from the instrument noise. The systematic error in this example originates from unaccounted scattering by aerosols emitted by the PP. It is assumed that the PP aerosol plume is perfectly correlated with the (3-dimensional) PP CO₂ plume. It is also assumed that an enhancement of 1% of the CO₂ column corresponds to an enhancement of the aerosol scattering optical depth of +0.5 (at 550 nm). The bottom middle panel shows the plume model fitted to the observations. The bottom right panel shows the “Model – observation” mismatch after the fit. The end results of the inversion are shown in the grey shaded box in the bottom right corner: The retrieved emission is $13.22 \pm 1.47 \text{ MtCO}_2/\text{yr}$. Also shown are the corresponding values of the second fit parameter (s), which accounts for a possible offset of the background column between the model and the observation (in this case there is no offset). Also listed are a number of important other parameters such as σ_v , which is the mean statistical uncertainty of the retrieved CO₂ column, or equivalently XCO₂ (here $\sigma_v=0.47\%$, i.e., approx. 2 ppm), meteorological parameters (wind speed, direction and horizontal mixing), and observation statistic results (maximum CO₂ column enhancement in percent relative to the background (here 1.78%) and the number of ground pixels where the enhancement is larger than a given factor times the 1-sigma XCO₂ retrieval precision σ_v). For this example the “CH₄-proxy method” has been used to obtain XCO₂. As can be seen, the systematic error of the retrieved emission is $0.22 \text{ MtCO}_2/\text{yr}$ ($13.22-13.0$).

are the “true plume” at high spatial resolution (bottom left panel), the “observed plume” at $2 \times 2 \text{ km}^2$ CarbonSat resolution (top left panel), the corresponding XCO₂ random error due to instrument noise (top middle panel), the assumed systematic error (in this case due to aerosols; see below for a detailed discussion; top right panel) and the difference between the model and the observations after the least-squares fit. The measurement directly over the PP is not used for the emission flux inversion to avoid potential problems with op-

tically thick water clouds originating from the PP emissions in the vicinity of the PP.

The main results of the inversion are shown in the grey shaded box in the bottom right corner of Fig. 6: The retrieved emission is $F_{\text{ret}}=13.22 \pm 1.47 \text{ MtCO}_2/\text{yr}$, i.e., the statistical uncertainty due to instrument noise is $1.47 \text{ MtCO}_2/\text{yr}$ (1-sigma) and the systematic error is $+0.22 \text{ MtCO}_2/\text{yr}$ ($=13.22-13.0$). The systematic error in this case is due to unconsidered aerosols in the PP plume. For the XCO₂ retrieval, a

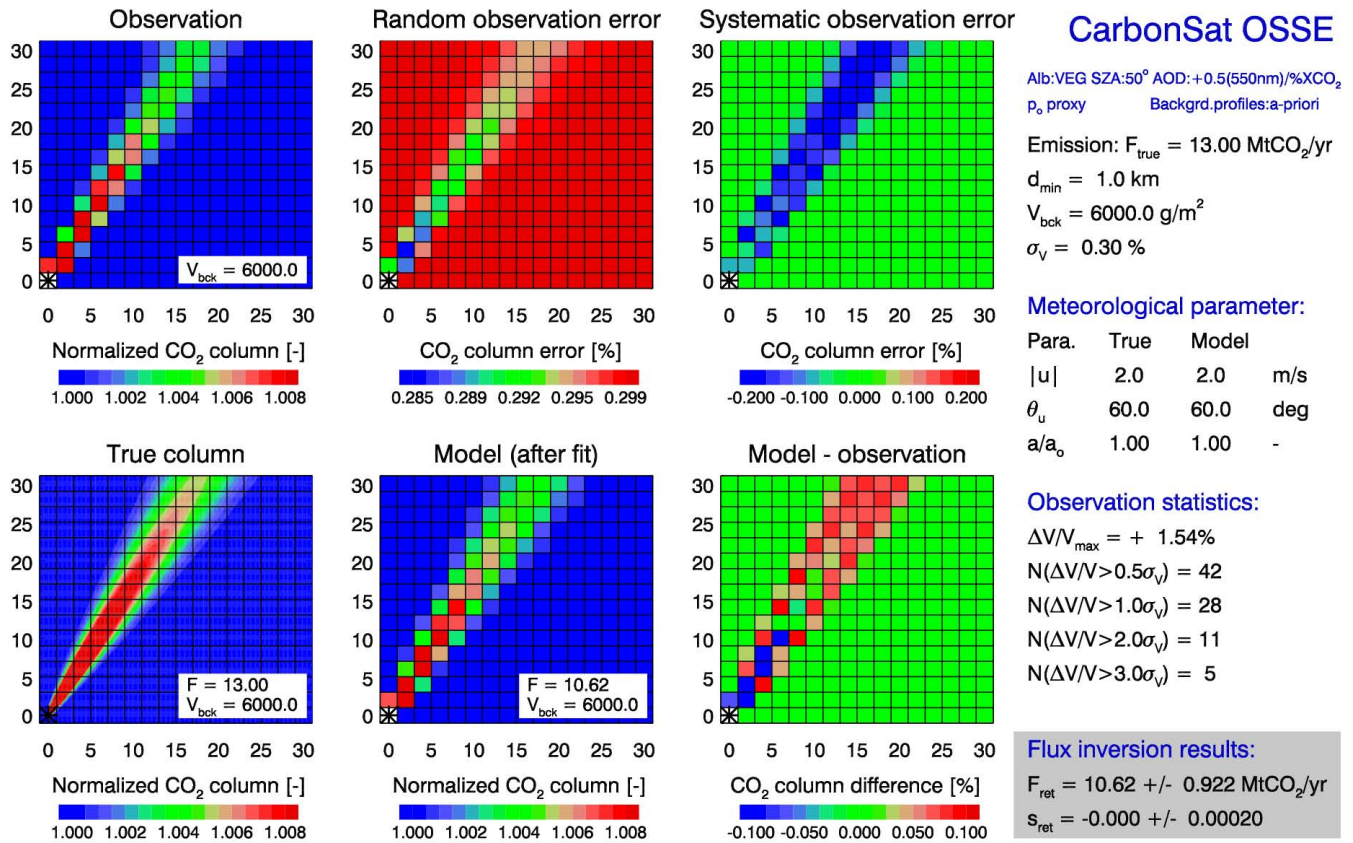


Fig. 7. As Fig. 6 but using the “p_o-proxy method” to obtain XCO₂. As can be seen, the XCO₂ retrieval precision is better compared to the “CH₄-proxy method” (here 0.3% compared to 0.47%, see Fig. 6) but the systematic error due to aerosols is larger (−2.38 compared to +0.22 MtCO₂/yr).

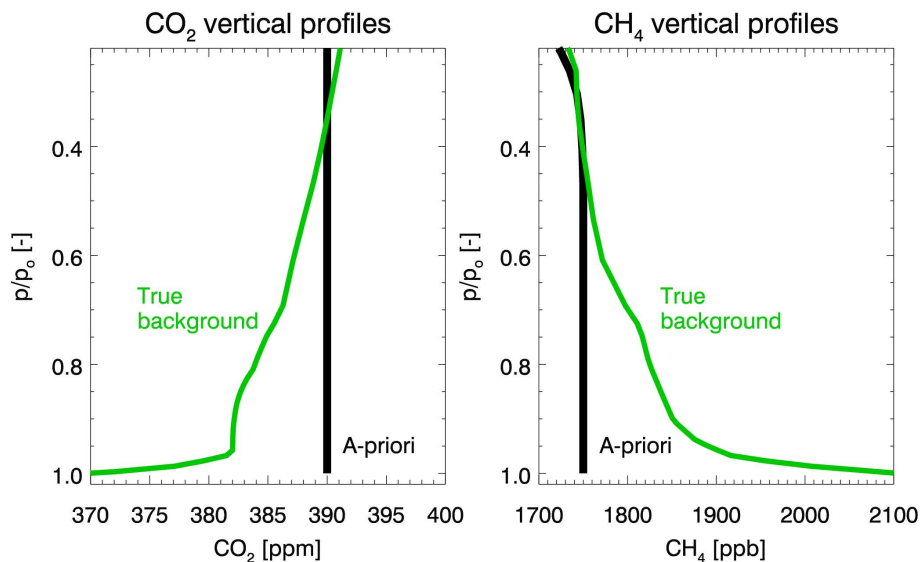


Fig. 8. Assumed background vertical profiles of CO₂ (left, green) and CH₄ (right, green) selected because they significantly differ from the corresponding a-priori profiles (black) used for XCO₂ and XCH₄ retrieval and because they also differ with respect to each other. They have been derived from CarbonTracker (Peters et al., 2007) and TM5 model data (Bergamaschi et al., 2007) and correspond to mid August, longitude 75° E, latitude 60° N.

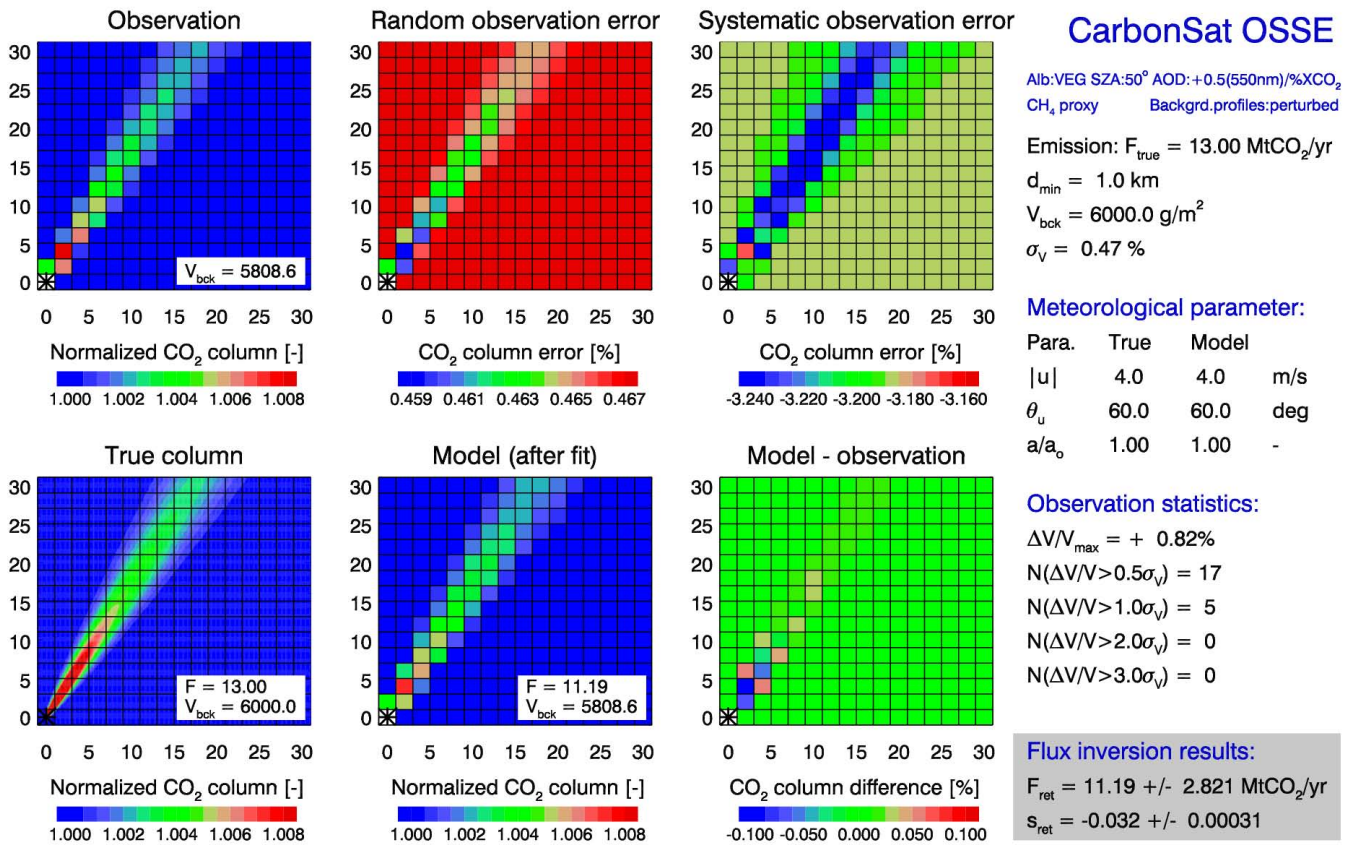


Fig. 9. As Fig. 6 but using the vertical profiles of CO₂ and CH₄ shown in green in Fig. 8 for generating the CarbonSat XCO₂ observations (the a-priori profiles used for the retrieval are the black profiles shown in Fig. 8). Here the true PP emission is 13 MtCO₂/yr, the wind speed is 4 m/s and the assumed aerosol OD enhancement is +0.5 per percent XCO₂ enhancement.

single constant default aerosol scenario has been used based on the (wrong) assumption that the PP is not emitting any aerosols. The default aerosol scenario is the one described in the caption of Table 3. For the simulation of the observed radiances, different aerosol scenarios have been defined for each individual measurement, i.e., for each of the $2 \times 2 \text{ km}^2$ ground pixels shown in Fig. 6. For the simulated measurements it has been assumed that the PP not only emits CO₂ but in addition aerosols and it has also been assumed that the PP aerosol plume is perfectly correlated with the CO₂ plume (a worst case situation) in the horizontal and in the vertical direction. It has been assumed that the aerosol scattering optical depth (OD) at 550 nm is enhanced by +0.5 for each percent XCO₂ (or CO₂ column) enhancement caused by the PP CO₂ emission. For the example shown in Fig. 6 the XCO₂ has been obtained using the “CH₄-proxy method”, which is supposed to be less sensitive to aerosol related errors compared to XCO₂ obtained using the “ p_o -proxy method”. This is confirmed by Fig. 7, which shows the corresponding results for the “ p_o -proxy method”. As can be seen, the systematic emission error is $-2.38 \text{ MtCO}_2/\text{yr}$ ($=10.62-13.0$), which is significantly larger than the $+0.22 \text{ MtCO}_2/\text{yr}$ obtained with the “CH₄-proxy method”.

How realistic is an increase of the aerosol scattering OD of +0.5 per percent XCO₂ enhancement? Prasad et al. (2006) have determined aerosol OD enhancements due to large PPs in India relative to their surroundings using MODIS data. Their Fig. 3 shows typical aerosol OD enhancements in the range 0.2–0.5 at 10 km resolution. As the spatial resolution of CarbonSat is higher, their findings cannot directly be used for this study. The aerosol OD enhancements can however roughly be estimated as follows: A typical lignite or hard coal fired PP emits about 1 kgCO₂ per kWh. This corresponds to 10 MtCO₂/yr for a PP which produces 10¹⁰ kWh electrical energy per year (1140 MW PP). Assuming that the emission factor of particulate matter with particles sizes less than 10 μm, i.e., PM₁₀, is 1 gPM₁₀/kWh (e.g., according to http://www.eoearth.org/article/Emissions_factors, 0.85 gPM₁₀/kWh is a typical value), then 1 gPM₁₀ is emitted per kgCO₂. The CO₂ background column is about 6 kgCO₂/m². A 1% CO₂ column enhancement therefore corresponds to 60 gCO₂/m². If 1 gPM₁₀ is emitted per kgCO₂, a CO₂ column enhancement of 1% or 60 gCO₂/m² corresponds to a PM₁₀ enhancement of 60 mgPM₁₀/m². Assuming that the vertical extent of the (well mixed) PP plume at some distance from the PP is 2 km, then 60 mgPM₁₀/m²

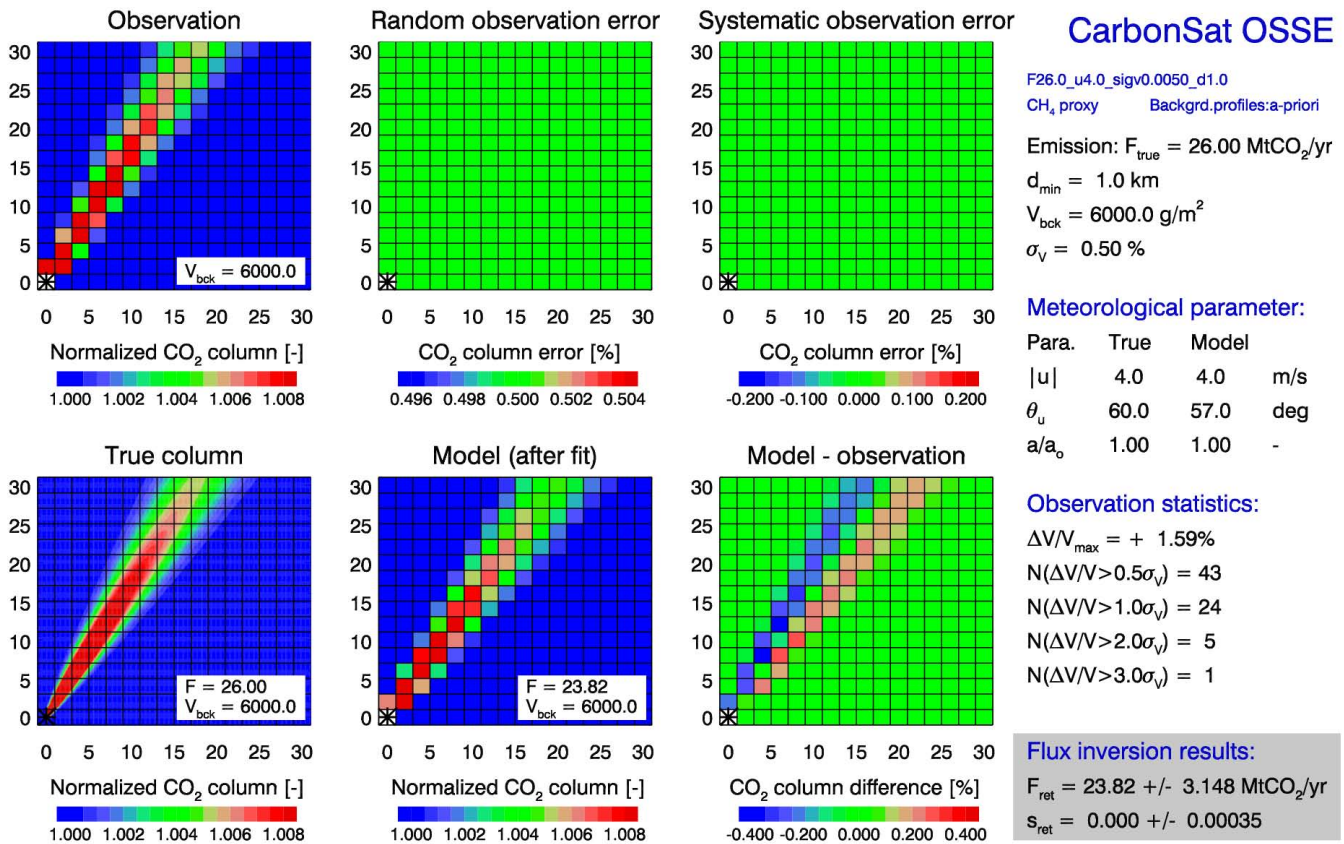


Fig. 10. OSSE results illustrating the effect of assuming a wrong wind direction, in this case 57° instead of 60°. As can be seen, this results in a characteristic mismatch between model and observation as shown in panel “Model – observation”. Here the true PP emission is 26 MtCO₂/yr and the wind speed is 4 m/s.

corresponds to a concentration of 30 μgPM₁₀/m³. Using the linear relation between PM₁₀ (in μgPM₁₀/m³) and aerosol OD (at 440 nm) reported by Péré et al. (2009) (i.e., PM₁₀=54×AOT+13), it follows that 30 μgPM₁₀/m³ roughly corresponds to an increase of the aerosol OD of 0.5. This shows that the assumption of an aerosol OD enhancement of 0.5 per percent CO₂ column enhancement is quite reasonable. Depending on the type of coal burned and other factors such as used filter technology, the aerosol emissions can probably be lower or larger. We therefore have also performed simulations assuming an aerosol OD enhancement of +2.0 per percent CO₂ column enhancement. The results are summarized in Table 4 (a detailed discussion is given below).

Our simulations show that aerosol related errors are lower if the “CH₄-proxy method” is used compared to the “p_o-proxy method” due to better cancellation of systematic errors when the CO₂ to CH₄ ratio is computed. The CH₄ background vertical profile is however not perfectly known and this is also true for the CO₂ background vertical profile. To quantify the corresponding error of the retrieved PP CO₂ emission we have generated synthetic observations using CO₂ and CH₄ vertical profiles, which are significantly

different from the a-priori profiles used for the retrieval and also differ with respect to each other. For this purpose vertical profiles of CO₂ and CH₄ have been extracted from global models using CarbonTracker for CO₂ (Peters et al., 2007) and TM5 for CH₄ (using scenario S1 from Bergamaschi et al., 2007). Figure 8 shows two profiles which differ significantly from the corresponding a-priori profiles and have an opposite vertical gradient. The corresponding PP emission flux errors which results from using these model profiles for the generation of the synthetic observations and assuming aerosol OD enhancements of +0.5 and +2.0 per percent CO₂ column enhancement, i.e., under very unfavorable (worst case) conditions for the retrieval, are listed in Table 4 (see also Fig. 9). The systematic PP emission flux error is 2.41 MtCO₂/yr (20% of 13 MtCO₂/yr) if the aerosol OD enhancement in the PP plume is +2.0 per percent CO₂ column enhancement if the “CH₄-proxy method” is used. The error is significantly larger when the “p_o-proxy method” is used. The “CH₄-proxy method” results in a systematic XCO₂ retrieval error as the assumed a-priori XCH₄ value differs from the true XCH₄ value (for the example shown in Fig. 9 the systematic error is –3.2%) but this offset is

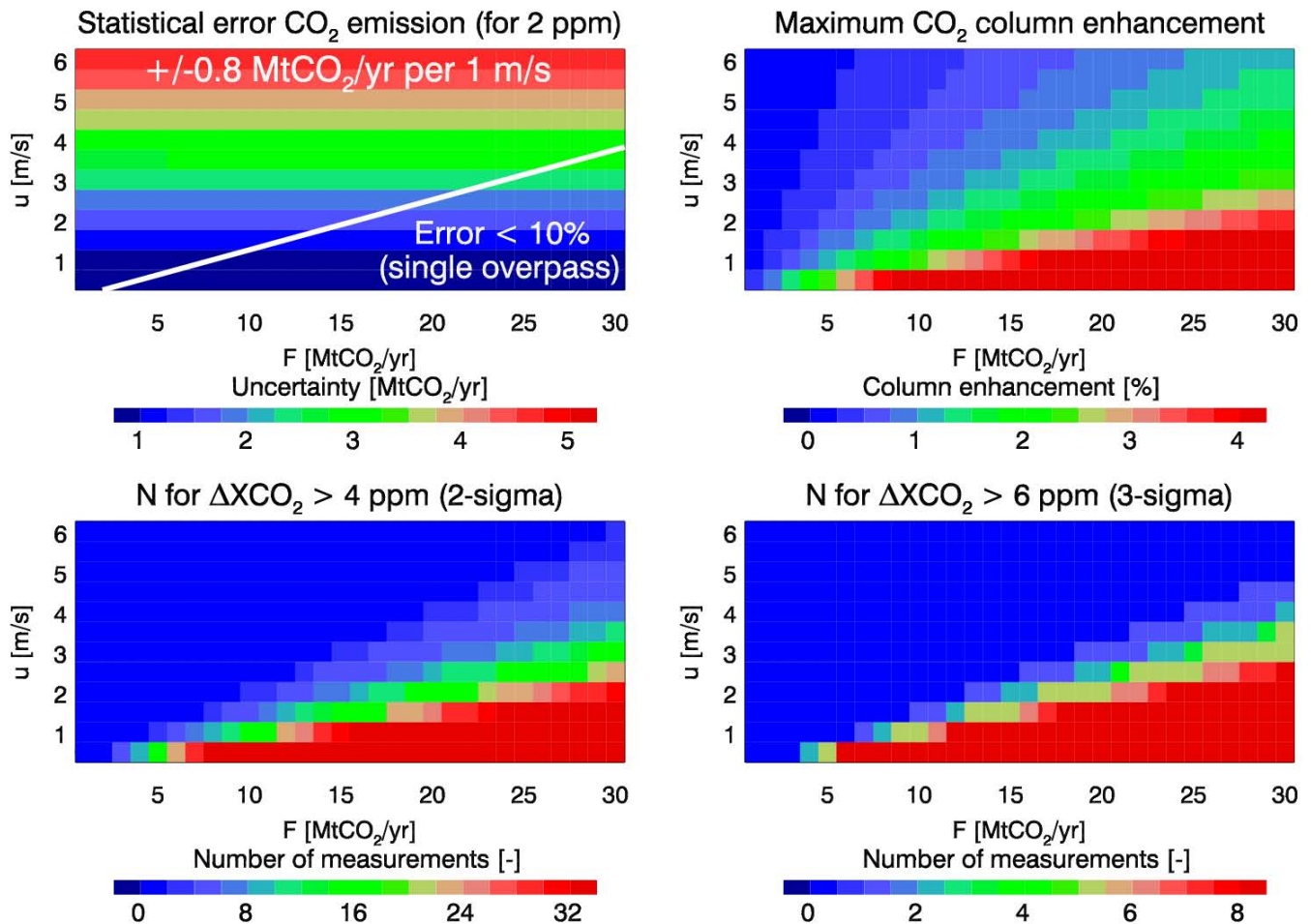


Fig. 11. Top left: Statistical error of the retrieved PP CO₂ emission as a function of the PP emission (x-axis) and wind speed (y-axis). Top right: Corresponding peak CO₂ column enhancement of the CO₂ emission plume. Bottom left: Number of ground pixels during single CarbonSat overflights where the CO₂ column enhancement is larger than 4 ppm. Bottom right: Number of ground pixels where the CO₂ enhancement is larger than 6 ppm. The assumed retrieval precision is 2 ppm (1-sigma).

nearly constant over the scene and compensated for by the CO₂ background column scaling parameter s , which is included in the least-squares fit to ensure that the inversion is insensitive to these kind of XCO_2 retrieval errors.

5.3.2 Errors due to clouds

For the results presented in this manuscript it is assumed that the scene around the PPs is sufficiently cloud free. CarbonSat can detect thick clouds for example by analysing the retrieved vertical columns of the three well mixed gases O₂, CO₂, and CH₄. If the retrieved columns of all three gases is significantly lower than the corresponding a-priori columns this is due to the shielding effect of clouds in the field of view. In order to enhance the sensitivity to clouds, especially to small (sub-pixel) clouds, CarbonSat is planned to be equipped with an additional instrument, the Cloud and

Aerosol Imager (CAI), which is supposed to be similar to the CAI onboard GOSAT (Kuze et al., 2009).

PBs however typically also emit significant amounts of water vapor which may condense and form water clouds in their vicinity. In order to avoid potential problems with optically thick water clouds originating from the PP itself, the measurement directly over the PP is typically not used in this study (see, e.g., Fig. 6). Typically the PP water cloud evaporates after a few hundred meters along the wind direction but it may happen that this cloud extends over more than one or two kilometers under certain conditions. We have therefore estimated to what extent the precision of the retrieved PP CO₂ emission is degraded when measurements closer than a given distance, d_{\min} , to the PP are rejected. The results are listed in Table 5. As can be seen, the precision gets only slightly worse even if all measurements within a radius of 4 km around the PP are rejected, i.e., not used for

Table 4. Systematic and random (1-sigma) errors of retrieved PP CO₂ emissions. The systematic errors are caused by neglecting PP aerosol emissions. The PP aerosol scattering vertical profile (i.e., the enhancement relative to a-priori aerosol background profile) is assumed to be perfectly correlated with the CO₂ profile enhancement originating from the PP CO₂ emission. The assumed enhancement of the aerosol scattering optical depth per 1% enhancement of X_{CO_2} relative to the background is listed in the first column. The assumed PP emission is 13 MtCO₂/yr. The measurement directly over the PP has not been used for the results shown here.

Aerosol enhancement (-)	Background profiles	Wind speed (m/s)	Retrieval method	Systematic error of retrieved PP emission (MtCO ₂ /yr)	Random error of retrieved PP emission (MtCO ₂ /yr)	Comment
0.5	A-priori	2	CH ₄ -proxy	+0.22 (1.7%)	1.47 (11.3%)	see Fig. 6
0.5	A-priori	2	p _o -proxy	-2.38 (18.3%)	0.92 (7.1%)	see Fig. 7
0.5	A-priori	4	CH ₄ -proxy	-1.40 (-10.8%)	2.95 (22.7%)	
0.5	A-priori	4	p _o -proxy	-4.77 (-36.7%)	1.86 (14.3%)	
0.5	See Fig. 8	4	CH ₄ -proxy	-1.81 (-13.9%)	2.82 (21.7%)	see Fig. 9
0.5	See Fig. 8	4	p _o -proxy	-4.74 (-36.5%)	1.87 (14.4%)	
2.0	See Fig. 8	4	CH ₄ -proxy	-2.41 (-18.5%)	2.74 (21.1%)	
2.0	See Fig. 8	4	p _o -proxy	-7.55 (-58.1%)	1.83 (14.1%)	

the emission flux inversion. This result was to be expected as the precision depends only weakly (square root dependence) on the number of measurements used for the least-squares fit.

5.3.3 Errors due to advection and mixing

A good knowledge of the wind speed is required for the PP CO₂ emission inversion. As can be seen from the formula for the Gaussian plume model given in Appendix A, the CO₂ column enhancement due to the PP emission depends on the ratio of the CO₂ emission (F) and the wind speed (u). The relative error of the inferred emission is therefore equal to the relative error of the wind speed. If the assumed wind speed is, for example, 10% too high, the retrieved emission will also be 10% too high. As shown in Table 6 this is confirmed by the simulated inversions.

Table 6 also lists the sensitivity of the retrieved emission with respect to wind direction and the parameter used for the parameterization of the horizontal mixing (parameter a defined in Appendix A). As can be seen, an error of the wind direction of 3° may result in an error of the retrieved emission of about 10%. In contrast to the wind speed, these type of errors result in a characteristic mismatch between the observed and the modeled plume. This is illustrated in Fig. 10 for the wind direction related mismatch. It is therefore reasonable to assume that these type of modeling errors can be detected and partially corrected.

5.3.4 Statistical uncertainty due to instrument noise

The statistical error of the retrieved PP emission due to instrument noise, i.e., the precision, depends on the wind speed. This is illustrated in Fig. 11, where the precision of the retrieved PP emission is shown as a function of PP emission and wind speed. The precision (1-sigma) is to a good

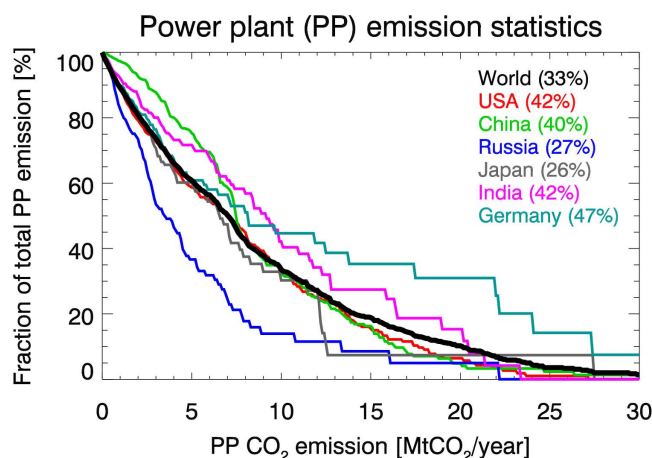


Fig. 12. Power plant (PP) emission statistics for selected countries and for the entire world. Shown is the fraction of a country's total PP emission emitted by PPs which emit more than a given amount. If, for example, only the emission of PPs which emit more than 5 MtCO₂/yr can be observed by CarbonSat this would mean that about 60% of the PP emissions in the USA could be captured. Also listed are the fraction of a country's PP emissions relative to the country's total anthropogenic CO₂ emission (see percentage values listed next to the country names). The emissions per country have been obtained from the BP data based (Statistical Review of World Energy, <http://www.bp.com>) and the PP emissions have been obtained from the CARMA data base (<http://carma.org>).

approximation 0.8 MtCO₂/yr per 1 m/s wind speed. The absolute value of the precision (in MtCO₂/yr) is independent of the PP emission but, of course, the relative error is the smaller the larger the PP emissions is. For large PPs (30 MtCO₂/yr) the statistical error is less than about 10% for wind speeds

CarbonSat daily orbital coverage (21 June)

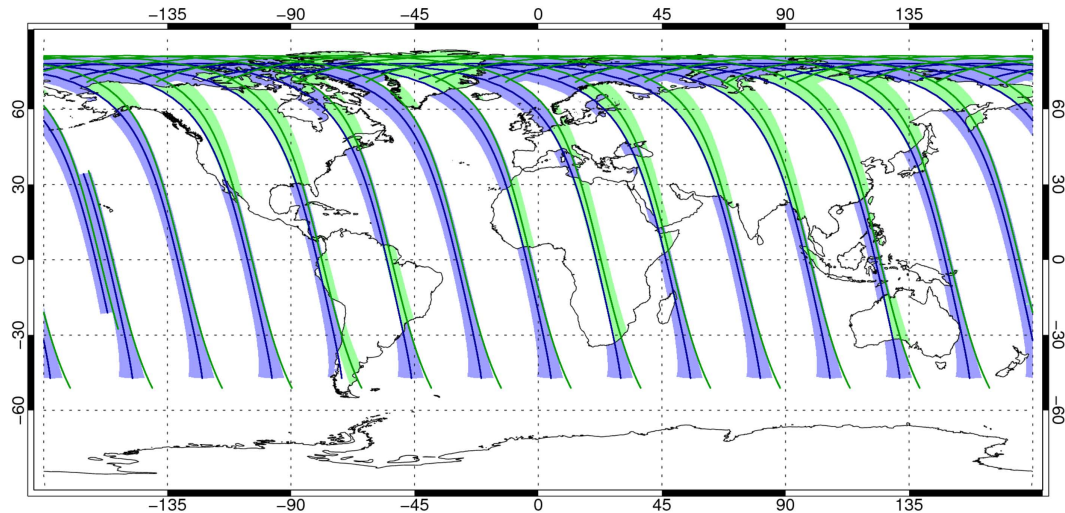


Fig. 13. CarbonSat orbital coverage for one day (21 June) for a swath width of 500 km corresponding to 250 across-track ground pixels of width 2 km each. Over land the main mode is the nadir mode (the coverage is shown in green) and over water the sun-glint mode (blue). All ground pixels on the day side are included up to a solar zenith angle of 80°.

Clear sky probability 16 x 16 km² (2008)

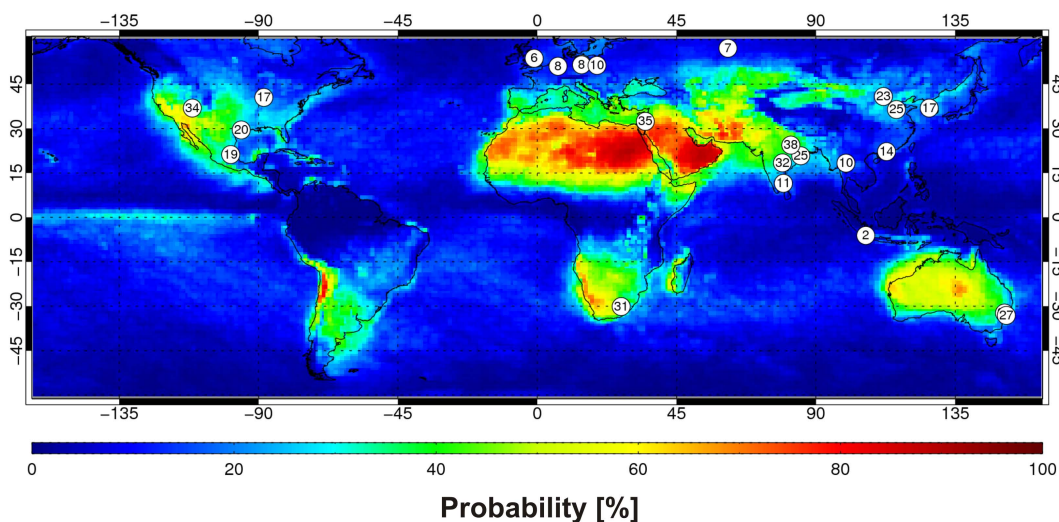


Fig. 14. Clear sky probability for 16×16 km² large scenes for one year (2008) obtained from the MODIS/Aqua cloud mask data product. The white circles show the positions of selected power plants (see also Table 7). The numbers in the circles show the numerical values of the clear sky probabilities in an area of 16×16 km² around the power plants.

up to 3–4 m/s but for smaller PPs (e.g., 5 MtCO₂/yr) the error may be larger than 10% even for wind speeds as low as 1 m/s. These precisions are valid for single PP overpasses and can be interpreted as CO₂ emission detection limit for PPs and other CO₂ point sources such as volcanoes.

Figure 11 also shows relevant additional information about the CO₂ plume as a function of PP emission and wind speed such as the maximum CO₂ column enhancement (in the

plume) and the number of CarbonSat measurements (ground pixels), where the CO₂ column enhancement is larger than two times or three times the noise level. If for a sufficiently large number of measurements the CO₂ column enhancement is larger than the noise, then the PP CO₂ plume will be clearly visible “by eye” when a map of the retrieved XCO₂ at the PP location and its surrounding is generated. This requirement is fulfilled for the conditions shown by the green

and red colors in the bottom panels of Fig. 11. These requirements are typically fulfilled if the statistical emission flux error is less than 10%.

The results shown in this section indicate that - depending on wind speed - the emission of moderate to strong PPs can typically be detected and quantified. Therefore the question arises how relevant it is if only large PPs can be monitored. To answer this, we have analyzed CO₂ emission data bases. Figure 12 shows PP emission statistics for several countries. PPs emitting more than 5 MtCO₂/yr are responsible for about 60% of the total PP emissions of the countries shown in Fig. 12. The emissions of PPs emitting 5 MtCO₂/yr can be quantified by CarbonSat probably only under low wind speed conditions (around 1 m/s). The results discussed so far correspond to single PP overpasses under (nearly) cloud free conditions. In order to estimate how many useful measurements can be obtained in a given time period, the expected number of sufficiently cloud free overpasses needs to be determined. This aspect is discussed in the next section.

6 Clear sky statistics for power plant overpasses

The satellite observations are based on reflected solar radiation, which cannot penetrate through thick clouds. Therefore sufficiently cloud free scenes are needed. To determine the probability for a sufficiently cloud free scene for CarbonSat PP overpasses, one year of high resolution (1 km) global MODIS/Aqua Collection 5 Level 2 Cloud Mask data products (Ackermann et al., 1998, 2008; Frey et al., 2008) has been analyzed. MODIS/Aqua has essentially the same orbit as assumed here for CarbonSat (sun-synchronous, Local Time Ascending Node (LTAN) 13:30). MODIS/Aqua is therefore well suited for this application. The daily orbital coverage of CarbonSat for one selected day is shown in Fig. 13 for illustration.

Figure 14 shows the resulting clear sky probabilities for the year 2008. The clear sky probabilities shown are valid for 16 km × 16 km large scenes, i.e., for given (PP) locations and their surroundings. As the MODIS/Aqua cloud masking algorithm is very strict, the results presented here are quite conservative. It is likely that scenes with partial cloud cover can also be used for PP emission monitoring. It needs to be investigated in a future study to what extent the strict filtering criteria used here can be relaxed to increase the number of useful observations.

Also shown in Fig. 14 are the locations of several PPs and the clear sky probability at their location. The numerical values are also listed in Table 7 along with the clear sky probabilities for the four seasons. PP names, locations and CO₂ emissions have been obtained from the CARMA data base (<http://carma.org>). As shown in Table 7, typical near-surface wind speeds for clear sky CarbonSat overpasses are in the range 2–6 m/s. As can also be seen from Table 7, typically 20 cloud free overpasses per year can be expected for a given power plant.

Table 5. Statistical uncertainties of the retrieved single overpass power plant (PP) CO₂ emissions (1-sigma) for different minimum distances (radii) around power plants (d_{\min}) defined to reject measurements in the vicinity of the PP which may be contaminated by optically thick (water) clouds originating from the PP emission. The assumed XCO₂ retrieval precision is 2 ppm.

PP emission (MtCO ₂ /yr)	Wind speed (m/s)	d_{\min} (km)	Uncertainty retrieved PP emission (MtCO ₂ /yr)
6.5	2	0	1.54 (23.7%)
6.5	2	1	1.57 (24.2%)
6.5	2	4	1.66 (25.5%)
6.5	4	0	3.06 (47.1%)
6.5	4	1	3.14 (48.3%)
6.5	4	4	3.31 (50.9%)
6.5	6	0	4.60 (70.8%)
6.5	6	1	4.71 (72.5%)
6.5	6	4	4.97 (76.5%)
13.0	2	0	1.54 (11.8%)
13.0	2	1	1.58 (12.2%)
13.0	2	4	1.67 (12.8%)
13.0	4	0	3.07 (23.6%)
13.0	4	1	3.15 (24.2%)
13.0	4	4	3.32 (25.5%)
13.0	6	0	4.60 (35.4%)
13.0	6	1	4.72 (36.3%)
13.0	6	4	4.97 (38.2%)
26.0	2	0	1.55 (6.0%)
26.0	2	1	1.59 (6.1%)
26.0	2	4	1.68 (6.5%)
26.0	4	0	3.08 (11.8%)
26.0	4	1	3.16 (12.2%)
26.0	4	4	3.33 (12.8%)
26.0	6	0	4.61 (17.7%)
26.0	6	1	4.73 (18.2%)
26.0	6	4	4.99 (19.2%)

7 Emissions from other point sources

In this section we shortly discuss the potential of CarbonSat to also detect and quantify the CO₂ and CH₄ emissions of point sources other than power plants.

Among other strong CO₂ point sources are, for example, large steel producing factories, that emit CO₂ in quantities which are comparable with the emissions by coal-fired PPs. It is estimated that more than 1 MtCO₂ per year is emitted for each Mt steel produced (Aichinger, 2007). Large steel producing factories produce several Mt steel per year and therefore are expected to emit several MtCO₂/yr.

Another category of strong point source CO₂ emitters are volcanoes. Certain volcanoes emit CO₂ in amounts comparable to coal-fired PPs. For example, the average 1975–1987 diffuse, i.e., non-eruptive, CO₂ emission of Mount Etna, Italy, is reported to be 13 MtCO₂/yr and the CO₂ emission of the Eyjafjalla volcano in Iceland is estimated to 150 000 tCO₂/day (55 MtCO₂/yr) during its eruptions in

Table 6. Errors of the retrieved power plant (PP) CO₂ emissions due to errors of the meteorological parameters wind speed (true value: 4 m/s), wind direction (true value: 60°) and horizontal mixing in the across wind direction (parameter *a*, see Appendix A; true value: *a*=104).

PP emission (MtCO ₂ /yr)	Wind speed error (%)	Wind direction error (deg)	Horiz.mixing error (%)	Error of retrieved PP emission (MtCO ₂ /yr)	Comment
13.0	+10.0	–	–	+1.3	
13.0	–10.0	–	–	–1.3	
13.0	–	+3	–	–1.0	
13.0	–	–3	–	–1.1	
13.0	–	–	+30	+1.3	
13.0	–	–	–30	–1.6	
26.0	+10.0	–	–	+2.6	
26.0	–10.0	–	–	–2.6	
26.0	–	+3	–	–2.0	
26.0	–	–3	–	–2.2	see Fig. 10
26.0	–	–	+30	+2.6	
26.0	–	–	–30	–3.3	

Table 7. Clear sky probabilities for CarbonSat overpasses over different selected power plants, ordered by latitude, for one entire year and for the four seasons December–February (DJF) to September–October (SON), derived from the MODIS/Aqua 2008 cloud mask data product. The clear sky probabilities are valid for 16 km×16 km large scenes. The power plant names, locations and emissions have been obtained from the CARMA data base (<http://carma.org>). Also listed are wind speed percentiles for cloud free CarbonSat overpasses obtained from ECMWF meteorological data (surface level, year 2008). *N* is the number of cloud free PP overpasses per year (here: 2008).

Power plant name	Country	CO ₂ emission (MtCO ₂ /yr)	Lat. (deg)	Long. (deg)	Year (%)	Clear sky probability (%)				Wind speed percentiles	<i>N</i>	
						DJF	MAM	JJA	SON	25% / 50% / 75% (m/s)		
REFTINSKAYA SDPP	Russia	22.2	57.1	61.6	7.0	1.6	8.3	12.4	5.7	1.9/2.7/3.9	30	
DRAX	UK	22.6	53.7	–1.0	6.8	15.9	4.7	1.9	4.9	3.1/6.0/8.4	15	
JANSCHWALDE	Germany	27.4	51.8	14.4	8.7	8.5	9.2	8.2	8.7	3.0/4.0/6.5	22	
SCHWARZE PUMPE	Germany	11.9	51.5	14.3	8.7	8.5	9.2	8.2	8.7	3.0/4.6/6.1	20	
BELCHATOW	Poland	34.6	51.3	19.3	10.0	7.6	6.8	14.8	10.8	4.3/4.9/6.1	20	
NIEDERASSEM	Germany	30.4	51.0	6.7	8.7	14.3	8.4	7.5	4.5	3.0/3.8/6.0	22	
TUOKETUO-1	China	24.7	40.8	111.8	23.6	9.2	20.6	23.7	40.5	4.0/5.2/6.1	33	
GIBSON	USA	22.4	40.5	–88.3	17.4	8.1	18.1	15.4	27.6	3.1/4.4/5.8	25	
NAVAJO	USA	19.1	36.9	–111.4	34.9	9.5	34.6	35.1	59.7	1.6/2.5/4.0	55	
TANGJIN	South Korea	24.7	36.9	126.6	17.3	17.8	26.1	8.8	16.7	1.8/2.9/4.1	22	
ZOUXIAN	China	34.5	36.4	116.0	25.2	19.7	34.5	11.5	34.8	2.0/3.4/4.5	28	
OROT RABIN	Israel	21.2	32.4	34.9	35.1	24.8	35.8	41.0	38.5	3.1/4.1/4.7	56	
WA PARISH	USA	20.9	29.5	–95.6	20.5	19.3	24.6	2.2	36.0	2.9/4.7/5.9	33	
VINDHYACHAL	India	20.2	24.4	81.9	38.1	73.5	38.8	0.0	41.5	1.0/1.8/3.4	29	
TAISHAN	China	19.6	22.2	112.8	14.1	32.6	5.4	0.3	19.2	2.1/2.9/4.1	11	
PETACALCO	Mexico	19.3	21.2	–99.0	19.7	34.3	29.9	1.8	13.0	1.5/2.3/3.1	25	
TALCHER STPS	India	23.4	20.8	85.1	25.4	58.8	23.4	0.1	20.9	0.8/1.1/2.1	22	
RAMAGUNDAM	India	21.4	18.4	79.2	32.1	69.1	30.6	0.0	28.7	1.9/2.5/3.2	34	
MAE MOH	Thailand	21.7	18.3	99.7	10.4	29.9	4.4	0.0	7.6	1.0/1.4/2.0	18	
NEYVELI	India	20.5	11.5	79.5	11.4	20.6	14.9	0.8	9.5	2.3/3.1/4.1	15	
SURALAYA	Indonesia	25.8	–6.1	106.1	2.8	0.2	1.2	8.9	1.1	2.2/3.8/4.4	8	
KENDAL	South Africa	26.8	–30.1	27.1	31.6	13.3	18.1	51.9	42.6	3.5/5.2/7.0	32	
BAYSWATER	Australia	19.8	–32.3	150.9	22.0	10.7	28.9	26.5	21.2	1.7/2.9/4.1	30	
ERARING	Australia	19.8	–33.1	151.5	27.4	17.8	35.6	29.1	26.6	2.6/3.6/4.2	25	
					Average:	19.1	21.9	19.7	12.9	22.0	ALL ≥ 1Mt: 2.0/3.2/4.8	

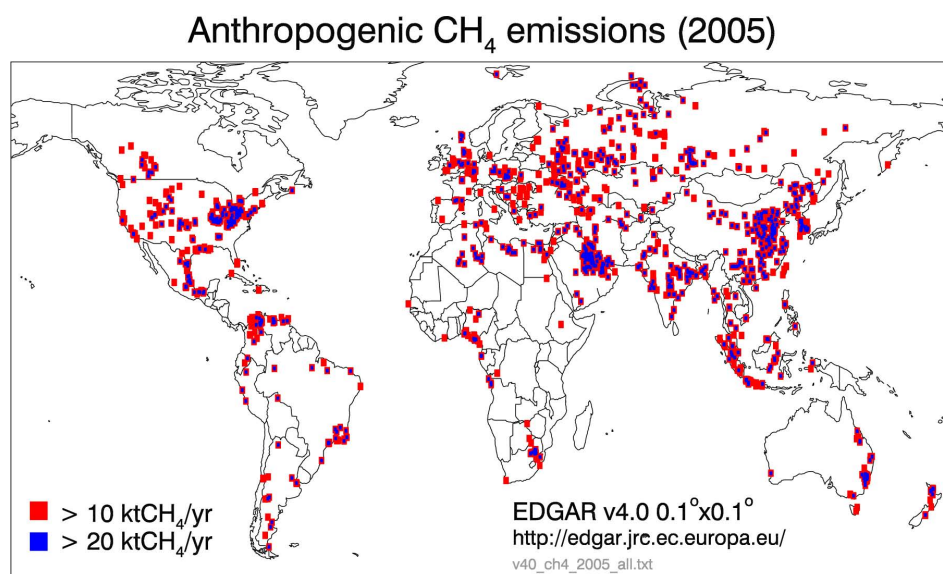


Fig. 15. Spatial distribution of strong localized anthropogenic methane sources according to the EDGAR data base (year 2005, gridded $0.1^\circ \times 0.1^\circ$). Shown are the locations of methane sources, which emit more than 10 ktCH₄/yr (red boxes) and more than 20 ktCH₄/yr (blue boxes). (Source: EC-JRC/PBL, EDGAR version 4.0, <http://edgar.jrc.ec.europa.eu/>, 2009).

April 2010 (see <http://www.informationisbeautiful.net/2010/planes-or-volcano/>).

In NRC (2010) the potential of OCO to detect and monitor the CO₂ emissions of more extended CO₂ sources such as large cities is discussed. Because of the better spatial coverage of CarbonSat due to its wider swath one can expect that the monitoring capability of CarbonSat is even better compared to OCO for these type of less localized targets.

CarbonSat also measures the second most important anthropogenic greenhouse gas, methane. Assuming that the methane point sources are well isolated in the sense that no strong CO₂ point sources such as coal-fired PPs are located in their surroundings, the “CO₂-proxy method” can be used to retrieve accurate XCH₄ (Frankenberg et al., 2005, 2008; Schneising et al., 2009). In this case XCH₄ is computed from the ratio of the retrieved CH₄ column and the simultaneously retrieved CO₂ column. The relative XCH₄ retrieval precision is therefore equal to the relative (i.e., percentage) XCO₂ retrieval precision obtained with the “CH₄ proxy method”. As can be seen from Table 3, this precision is typically 0.5% or better, which corresponds to 8 ppb for XCH₄. OSSE for methane emission inversion similar as the ones presented here for CO₂ have also been conducted for CH₄. As for CO₂, the corresponding XCH₄ or CH₄ column enhancement relative to the background due to the localized CH₄ source must be on the order of 1% in order to be clearly detectable by single CarbonSat overpasses. The OSSE show that the statistical uncertainty of the inferred CH₄ emission for a retrieval precision of 8 ppb (0.5%) is 1.4 ktCH₄/yr per 1 m/s wind speed, i.e., in the range 3–8 ktCH₄/yr for typical wind speeds in the range 2–6 m/s.

CarbonSat has therefore the potential to detect and quantify the CH₄ emission of various natural and anthropogenic methane “hot spot” emission sources, for example:

- landfills and coal mines (e.g., the European Pollutant Release and Transfer Register (<http://prtr.ec.europa.eu/PollutantReleases.aspx>) lists many sites in Europe where methane emissions are estimated to be significantly larger than 10 ktCH₄/yr),
- pipeline compressor stations (e.g., Dedikov et al. (1999) report emissions on the order of 10 ktCH₄/yr),
- oil sand areas (e.g., Siddique et al. (2008) estimate that the highly variable methane emissions in the oil sand areas of Alberta, Canada, may significantly exceed 10 ktCH₄/yr),
- oil and gas fields (e.g., Yamal West Siberian Gas Fields (for example Jagovkina et al. (2000) report methane column enhancements of 1–2% over several kilometer), Prudhoe Bay Oil Field, Alaska, USA, or Gulf of Mexico (for example Villasenor et al. (2003) report methane emissions up to 14 ktCH₄/yr per platform)),
- marine seeps (e.g., Coal Oil Point, Santa Barbara, California, USA (Leifer et al. (2006a,b) report emissions larger than 1 m³CH₄/s in a region of several square kilometers corresponding to about 20 ktCH₄/yr) or Black Sea seeps off the coast of Georgia (e.g., Judd (2004) report emissions of more than 400 kgCH₄/s/m³ over an area of about 10⁵m² corresponding to about 40 ktCH₄/yr)),

- degassing marine shelf areas (e.g., Shakhova et al. (2010) report boundary layer methane enhancements in the Eastern Siberian Arctic Shelf of up to 8 ppm over a distance of more than 100 km),
- mud volcano eruptions (e.g., Kourtidis et al. (2006) show that corresponding emissions may result in methane column enhancements relative to the background which may even be detectable with SCIAMACHY despite much larger ground pixel size (30×60 km²) compared to CarbonSat (2×2 km²)).

Figure 15 shows the spatial distribution of strong localized anthropogenic methane sources according to the EDGAR database. Shown are all methane sources (at 0.1°×0.1° resolution) which emit more than 10 and more than 20 ktCH₄/yr, i.e., significantly more than the CarbonSat detection limit.

Therefore CarbonSat has the potential to be an important tool for the detection and monitoring of many “hot spot” greenhouse gas emission sources in addition to coal-fired power plants.

8 Conclusions

A satellite remote sensing technology has been discussed, which enables the detection and monitoring of CO₂ emissions from strong localized CO₂ sources such as coal-fired power plants.

The instrument concept is based on an imaging spectrometer system which measures high resolution spectra of reflected solar radiation in the SWIR/NIR spectral region in nadir (and sun-glint) mode covering relevant absorption bands of CO₂, CH₄ and O₂ (to obtain surface pressure, p_o) at high spatial resolution. The instrument concept is similar to the concept developed for OCO and GOSAT but has been optimized especially to serve important additional applications such as monitoring of localized CO₂ and CH₄ sources. This is achieved by a unique combination of wide swath imaging (500 km swath) and small ground pixel size (2×2 km²).

Observing System Simulation Experiments (OSSE) have been conducted to estimate random and systematic errors of the inferred power plant emissions. The OSSE comprise radiative transfer and instrument simulation and inversion of the synthetic measurements (radiance spectra) to obtain vertical columns of CO₂ and CH₄ as well as surface pressure. From these retrieved quantities dry air column-averaged mixing ratios of CO₂, denoted X_{CO_2} , have been obtained using two different methods (“ p_o -proxy method” and “CH₄-proxy method”). The retrieved X_{CO_2} and its error has been used to obtain power plant emissions including error estimates via inverse modeling. A Gaussian plume model has been used to simulate the CO₂ column enhancement resulting from the power plant CO₂ emission.

It has been shown that power plant CO₂ emissions can be unequivocally detected and quantified. The estimated sta-

tistical uncertainty of the inferred power plant CO₂ emission due to instrument (detector) noise is 0.8 MtCO₂/yr (1-sigma) per 1 m/s wind speed for a single power plant overpass, i.e., in the range 1.6–4.8 MtCO₂/yr for typical near-surface fair weather wind speeds in the range 2–6 m/s. This corresponds to 12–36% of the emission of mid-size power plants (13 MtCO₂/yr) or to 6–18% of the emission of large power plants (26 MtCO₂/yr). Using clear sky statistics it has been conservatively estimated that typically 20 sufficiently cloud free overpasses over a given power plant per year can be expected.

The sensitivity to several parameters has been determined which are expected to result in systematic errors such as unaccounted aerosols and optically thick water clouds originating from the power plant emission and transport related errors due to imperfect knowledge of wind speed, wind direction and horizontal mixing. The most relevant transport related error source is wind speed. For the Gaussian plume model the relative systematic error of the inferred emission is equal to the relative error of the wind speed, i.e., a 10% overestimation of the wind speed results in a 10% overestimation of the inferred emission. Optically thick water clouds in the vicinity of the power plant arising from the PP emission can be dealt with by excluding measurements within a certain radius around the power plant from the analysis. An important error source is unaccounted or not properly accounted scattering due to aerosols (particulate matter) emitted by the power plant in addition to CO₂. It has been found that neglecting aerosols in the PP emission plume results in systematic errors in the range 0.2–2.5 MtCO₂/yr, depending on PP aerosol emission, for a PP emitting 13 MtCO₂/yr.

The investigated satellite, called Carbon Monitoring Satellite (CarbonSat), is not limited to this application but can also contribute to the detection and quantification of a number of other important localized CO₂ emission sources such as volcanoes and steel factories as well as a large number of natural and anthropogenic localized CH₄ emission sources such as land fills, oil and gas fields, pipeline leaks, coal mines, mud volcanoes and marine seeps. The estimated precision of the inferred CH₄ emission is 1.4 ktCH₄/yr (1-sigma) per 1 m/s wind speed for a single overpass for an X_{CH_4} retrieval precision of 8 ppb (0.5%), which can be achieved in most cases (for measurements over land; measurements over water using CarbonSat’s sun-glint mode have not been discussed in this manuscript).

In addition to greenhouse gas emission hot spot detection and monitoring, the CarbonSat satellite mission aims at fulfilling all relevant requirements for global regional-scale CO₂ and CH₄ surface flux inverse modeling, i.e., it fulfills similar requirements as have been identified for the dedicated greenhouse gas missions OCO and GOSAT.

The discussed satellite concept has the potential to become an important component of a future global CO₂ and CH₄ emission monitoring system, which is needed for example

for independent verification of reported emissions in the context of, for example, Kyoto protocol follow-on agreements.

CarbonSat could continue the time series of global greenhouse gas (CO₂, CH₄) observations from space which started with the launch of ENVISAT with the SCIAMACHY instrument on board in 2002. This time series is currently being continued by the Japanese GOSAT satellite (launched in January 2009) and possibly will be extended for CO₂ with OCO-2 (2013–2015). There is however high risk for an observational gap in the time period 2016 to 2020 or later. This gap can be closed with a satellite mission similar to the one investigated in this study.

The presented concept is based on a single satellite but the spatio-temporal coverage can of course be significantly improved if the space based greenhouse gas monitoring system would consist of a constellation of greenhouse gas observing satellites. This is important especially if emissions of time dependent emission sources need to be quantified with high precision. In this context it may be possible to also use satellite instruments less complex (and therefore less expensive) than the one discussed here. These “compact satellites” may only cover one band, the SWIR-1 band, which covers absorption lines of CO₂ and CH₄ around 1.6 μm. Such “compact satellites” are expected to deliver very useful information on localized CO₂ and CH₄ sources (using the “CH₄-proxy method” or the “CO₂-proxy method”, depending on emission target) and can also be expected to provide very useful data for global regional-scale CH₄ surface flux inversions as demonstrated by SCIAMACHY (Frankenberg et al., 2005, 2008; Bergamaschi et al., 2009; Schneising et al., 2009). “Compact satellites” will however probably not be able to provide a sufficient data quality as needed for the global regional-scale CO₂ surface flux inversion application.

Appendix A

Gaussian plume model

In order to simulate the CO₂ vertical column enhancement at and downwind of a CO₂ source such as a CO₂ emitting power plant, a quasi-stationary Gaussian plume model is used (Sutton, 1932). Integrated for the total vertical column V it equals:

$$V(x, y) = \frac{F}{\sqrt{2\pi}\sigma_y(x)u} e^{-\frac{1}{2}\left(\frac{y}{\sigma_y(x)}\right)^2}, \quad (\text{A1})$$

where V is the CO₂ vertical column (in g/m²) at and downwind of the point source. The x -direction is parallel to the wind direction and the y -direction perpendicular to the wind direction. V depends on the emission rate F (in g/s), the across wind distance y , wind speed u , and the standard deviation in y direction, σ_y . The standard deviation $\sigma_y = \sigma_y(x)$ is a function of the along wind distance x and depends on the

atmospheric stability parameter a (Masters, 1998, and references therein):

$$\sigma_y(x) = a \cdot x^{0.894}. \quad (\text{A2})$$

Here x must be specified in kilometers to give σ_y in meters. For stability class C (slightly unstable) Masters (1998) gives:

$$a = 104. \quad (\text{A3})$$

To simulate an emission source with a cross section y_0 at the plume's origin an offset x_0 is added to Eq. (A2):

$$\sigma_y(x) = a (x + x_0)^{0.894}, \quad (\text{A4})$$

where:

$$x_0 = \left(\frac{y_0}{a}\right)^{\frac{1}{0.894}}. \quad (\text{A5})$$

Appendix B

Atmospheric CO₂ retrieval algorithm

Here we provide a description of the retrieval algorithm which has been used for this study. This retrieval algorithm is the “Bremen optimal ESTimation DOAS” (BESD) algorithm. BESD is based on Optimal Estimation (OE) (Rodgers, 2000) and on “Differential Optical Absorption Spectroscopy” (DOAS) (see, e.g., Buchwitz et al., 2000b, and references given therein). OE allows to constrain the retrieval using uncertain a-priori information, e.g., on aerosols and (thin) clouds. DOAS permits to filter out disturbing low frequency radiance contributions which are typically difficult to model such as contributions from aerosol scattering, changes of the Earth's surface spectral reflectance and changes of instrument calibration functions. BESD is under development for improved SCIAMACHY CO₂ retrieval (Buchwitz et al., 2009; Reuter et al., 2010).

The satellite instrument measures radiance spectra $R_i \equiv R(\lambda_i)$ in nadir mode at discrete wavelengths λ_i as well as the solar irradiance, $F_i \equiv F(\lambda_i)$. For the following we assume that the wavelength grids of the nadir and the solar spectra are either identical or that the solar spectrum has been interpolated onto the wavelength grid of the nadir measurements. The directly measured quantities R_i and F_i are used to compute the measured sun-normalized radiance or intensity I_i which is defined as $I_i \equiv \pi R_i / F_i$. In the following the measurement vector \mathbf{y} is used whose elements are $y_i \equiv \ln(I_i)$. The corresponding model quantity \mathbf{y}^{mod} is obtained with the radiative transfer model (RTM) SCIATRAN (Buchwitz et al., 2000a; Rozanov et al., 2002). The version of BESD used for this study is based on linearizing the logarithm of the sun-normalized radiance around an assumed (atmospheric) state denoted by the a priori state vector \mathbf{x}_a , i.e., the following equation is used for \mathbf{y}^{mod} as a function of state vector \mathbf{x} :

$$\mathbf{y}^{\text{mod}}(\mathbf{x}) = \mathbf{y}_a + \mathbf{K}(\mathbf{x} - \mathbf{x}_a). \quad (\text{B1})$$

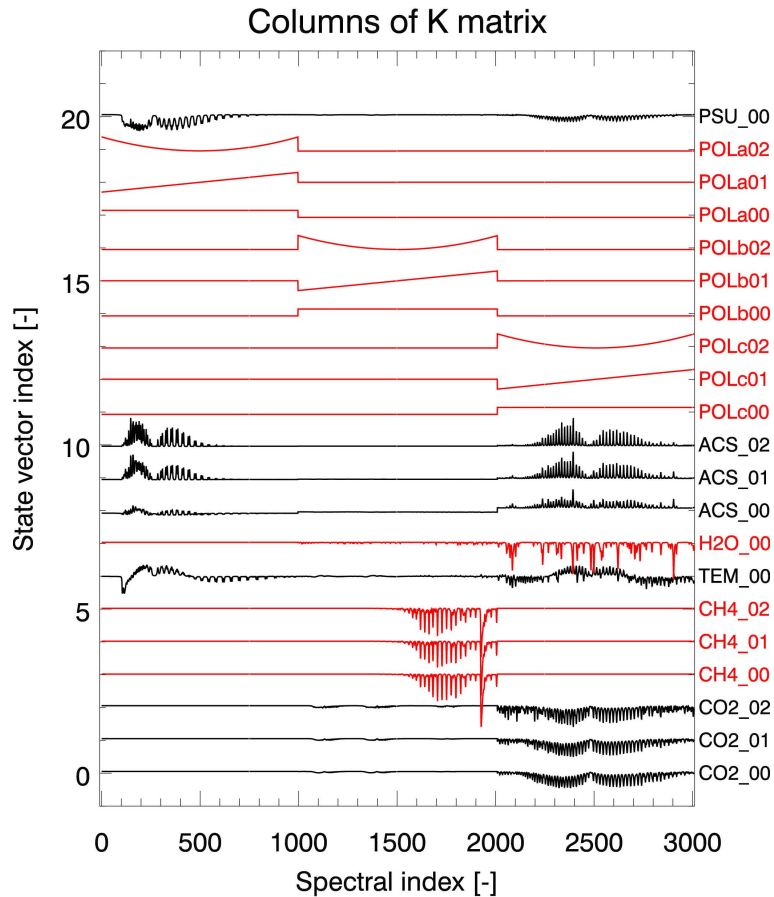


Fig. B1. Visualization of a typical retrieval Jacobian (\mathbf{K}) matrix. Each spectrum shows the (scaled and shifted) derivative of the logarithm of the sun-normalized radiance due to a change of the corresponding state vector element. The state vector element identifiers are shown on the right hand side. For an explanation of the state vector elements see main text and Table B1.

Here $\mathbf{y}_a \equiv \mathbf{y}^{\text{mod}}(\mathbf{x}_a)$, i.e., \mathbf{y}_a is the logarithm of the sun-normalized radiance for state vector \mathbf{x}_a . Matrix \mathbf{K} is the Jacobian matrix with elements $K_{ij} = f_j \partial y_i^{\text{mod}} / \partial x_j |_{\mathbf{x}=\mathbf{x}_a}$. For numerical reasons (most of) the elements of the Jacobian matrix are defined to be dimensionless. They express the relative change of the intensity due to a relative change of state vector element j (unit: %/%). For these cases $f_j = x_j$ and K_{ij} can be interpreted as the relative change of the intensity at wavelength λ_i due to a relative change of state vector element j . This is true for all state vector elements except for the elements which correspond to the coefficients of the low order polynomials. The low order polynomial is included to make the retrieval less sensitive to spectrally broadband radiance (and/or measured signal) contributions which typically cannot be modelled with high accuracy. For the polynomial coefficient x_j the corresponding elements of the Jacobian matrix are: $K_{ij} = ((\lambda_i - \lambda_c) / \lambda_c)^{n_p}$, where λ_c is the center wavelength of the spectral fitting window for which the polynomial is valid. n_p is an integer in the range $0, \dots, N_p$, where N_p is the order of the polynomial (here we use a quadratic polynomial, i.e., $N_p=2$).

The columns of the Jacobian matrix \mathbf{K} for a typical RT simulation are shown in Fig. B1. Each column of \mathbf{K} corresponds to one state vector element. The state vector elements and their assumed a-priori uncertainties are listed in Table B1. For the retrieval, a 3-layer atmosphere is used (the RT simulations are however performed on a finer vertical grid). The three layers are denoted “Lower Troposphere” (LT), “Upper Troposphere” (UT), and “Stratosphere” (ST). As can be seen from Table B1, 21 state vector elements have been defined. For CO₂ and CH₄ their sub-columns (layer columns) in the three atmospheric layers are state vector elements. For each of the three layers a dimensionless scattering parameter has been defined, the layers aerosol and cloud scattering (ACS) optical depth. Additional parameters are scaling factors for the temperature (TEM) and water vapour (H₂O) vertical profiles, a scaling parameter for the pressure profile (“surface pressure” parameter PSU) and nine parameters for the three second order polynomials in the three spectral bands (parameters POL). The Optimal Estimation method requires a-priori uncertainties to be assigned to each parameter and the corresponding values, which are to be

interpreted as 1-sigma relative uncertainties, are also listed in Table B1. The two variance/covariance matrices \mathbf{S}_{x_a} and \mathbf{S}_y are assumed to be diagonal matrices, i.e., they are fully specified by the uncertainties (standard deviations) listed in Table B1.

BESD is based on minimizing the following cost function $C(\mathbf{x})$:

$$C(\mathbf{x}) = (\mathbf{x} - \mathbf{x}_a)^T \mathbf{S}_{x_a}^{-1} (\mathbf{x} - \mathbf{x}_a) + (\mathbf{y} - \mathbf{y}^{\text{mod}}(\mathbf{x}))^T \mathbf{S}_y^{-1} (\mathbf{y} - \mathbf{y}^{\text{mod}}(\mathbf{x})). \quad (\text{B2})$$

Here \mathbf{x} is the to be estimated (atmospheric) state vector at the time of the measurement, \mathbf{x}_a is the assumed a-priori state vector (ideally the climatological mean) with a-priori variance/covariance matrix \mathbf{S}_{x_a} , \mathbf{y} is the measurement vector with variance/covariance matrix \mathbf{S}_y , and $\mathbf{y}^{\text{mod}}(\mathbf{x})$ is the forward model which relates the desired but unknown state vector with the directly measured quantity. Here $()^T$ denotes matrix transpose and $()^{-1}$ denotes matrix inverse.

The solution of this estimation problem is an estimate of the state vector, denoted $\hat{\mathbf{x}}$, and its variance/covariance matrix $\hat{\mathbf{S}}_x$. How this solution can be obtained is shortly described in the following (for details see (Rodgers, 2000; Rodgers and Connor, 2003) and references given therein).

It can be shown that the state vector covariance matrix for the absolute state vector elements, $\hat{\mathbf{S}}_x^a$, can be obtained from the state vector covariance matrix for the relative state vector elements, $\hat{\mathbf{S}}_x$, as follows:

$$\left(\hat{\mathbf{S}}_x^a\right)_{ij} = \left(\bar{x}_i^a \bar{x}_j^a\right) \left(\hat{\mathbf{S}}_x\right)_{ij}. \quad (\text{B3})$$

Analogous relations exist for the smoothing error covariance matrix

$$\left(\hat{\mathbf{S}}_S^a\right)_{ij} = \left(\bar{x}_i^a \bar{x}_j^a\right) \left(\hat{\mathbf{S}}_S\right)_{ij} \quad (\text{B4})$$

and the measurement noise covariance matrix

$$\left(\hat{\mathbf{S}}_{yx}^a\right)_{ij} = \left(\bar{x}_i^a \bar{x}_j^a\right) \left(\hat{\mathbf{S}}_{yx}\right)_{ij}. \quad (\text{B5})$$

Assuming Gaussian statistics and a linear forward model, which relates the state vector \mathbf{x} to the measured quantity \mathbf{y} via $\mathbf{y} = \mathbf{y}^{\text{mod}}(\mathbf{x}) + \epsilon$, where ϵ is the measurement error, the solution of this estimation problem, $\hat{\mathbf{x}}$, can be formulated in terms of the retrieval gain matrix \mathbf{G} :

$$\hat{\mathbf{x}} = \mathbf{x}_a + \mathbf{G}(\mathbf{y} - \mathbf{y}_a). \quad (\text{B6})$$

Gain matrix \mathbf{G} is defined as

$$\mathbf{G} = \frac{d\hat{\mathbf{x}}}{d\mathbf{y}} = \hat{\mathbf{S}}_x \mathbf{K}^T \mathbf{S}_y^{-1}. \quad (\text{B7})$$

Here $\hat{\mathbf{S}}_x$ is the uncertainty covariance matrix of $\hat{\mathbf{x}}$ and is given by

$$\hat{\mathbf{S}}_x = (\mathbf{K}^T \mathbf{S}_y^{-1} \mathbf{K} + \mathbf{S}_{x_a}^{-1})^{-1}. \quad (\text{B8})$$

Table B1. BESD retrieval algorithm state vector elements and a-priori uncertainties. PSU is the surface pressure state vector element with corresponding 1-sigma uncertainty of 3%. The nine POL parameters are the coefficients of the quadratic polynomials in the three spectral bands. ACS are the three state vector elements for aerosol and cloud scattering in the three atmospheric layers stratosphere (ST), upper troposphere (UT) and lower troposphere (LT). In the three bottom rows the CO₂ state vector elements are listed, which are layer columns. The assumed 1-sigma uncertainty of the CO₂ lower tropospheric layer column (ID CO2_00) is 6%. Stronger constraints are used for CO₂ in the upper layers. For CH₄ the constraints are relaxed as methane is assumed to be more variable than CO₂. For H₂O and temperature single vertical profile scaling factors have been defined as state vector elements.

Number	ID	Explanation	Uncertainty (relative) (—)
20	PSU.00	Surface pressure	0.030
		Polynom NIR	
19	POLa02	Quadratic term	1000.0
18	POLa01	Linear term	1000.0
17	POLa00	Constant term	1000.0
		Polynom SWIR-1	
16	POLb02	Quadratic term	1000.0
15	POLb01	Linear term	1000.0
14	POLb00	Constant term	1000.0
		Polynom SWIR-2	
13	POLc02	Quadratic term	1000.0
12	POLc01	Linear term	1000.0
11	POLc00	Constant term	1000.0
10	ACS_02	Aero./clouds scat. ST	0.050
9	ACS_01	Aero./clouds scat. UT	5.000
8	ACS_00	Aero./clouds scat. LT	1.000
7	H2O.00	H ₂ O(z) scaling	2.000
6	TEM.00	$T(z)$ scaling	0.100
5	CH4.02	CH ₄ ST	0.010
4	CH4.01	CH ₄ UT	0.060
3	CH4.00	CH ₄ LT	0.120
2	CO2.02	CO ₂ ST	0.005
1	CO2.01	CO ₂ UT	0.030
0	CO2.00	CO ₂ LT	0.060

An important matrix for the characterization of the retrieval is the averaging kernel matrix \mathbf{A} , which can be formulated in terms of \mathbf{G} and Jacobian matrix \mathbf{K} :

$$\mathbf{A} = \frac{d\hat{\mathbf{x}}}{d\mathbf{x}} = \frac{d\hat{\mathbf{x}}}{d\mathbf{y}} \frac{d\mathbf{y}}{d\mathbf{x}} = \mathbf{G}\mathbf{K}, \quad (\text{B9})$$

where \mathbf{x} is the true state vector (which is only exactly known for simulations).

The sum of the diagonal elements of \mathbf{A} is the so-called degree of freedom for signal $ds = \text{trace}(\mathbf{A})$, which can be interpreted as the number of “independent pieces of information” which can be retrieved.

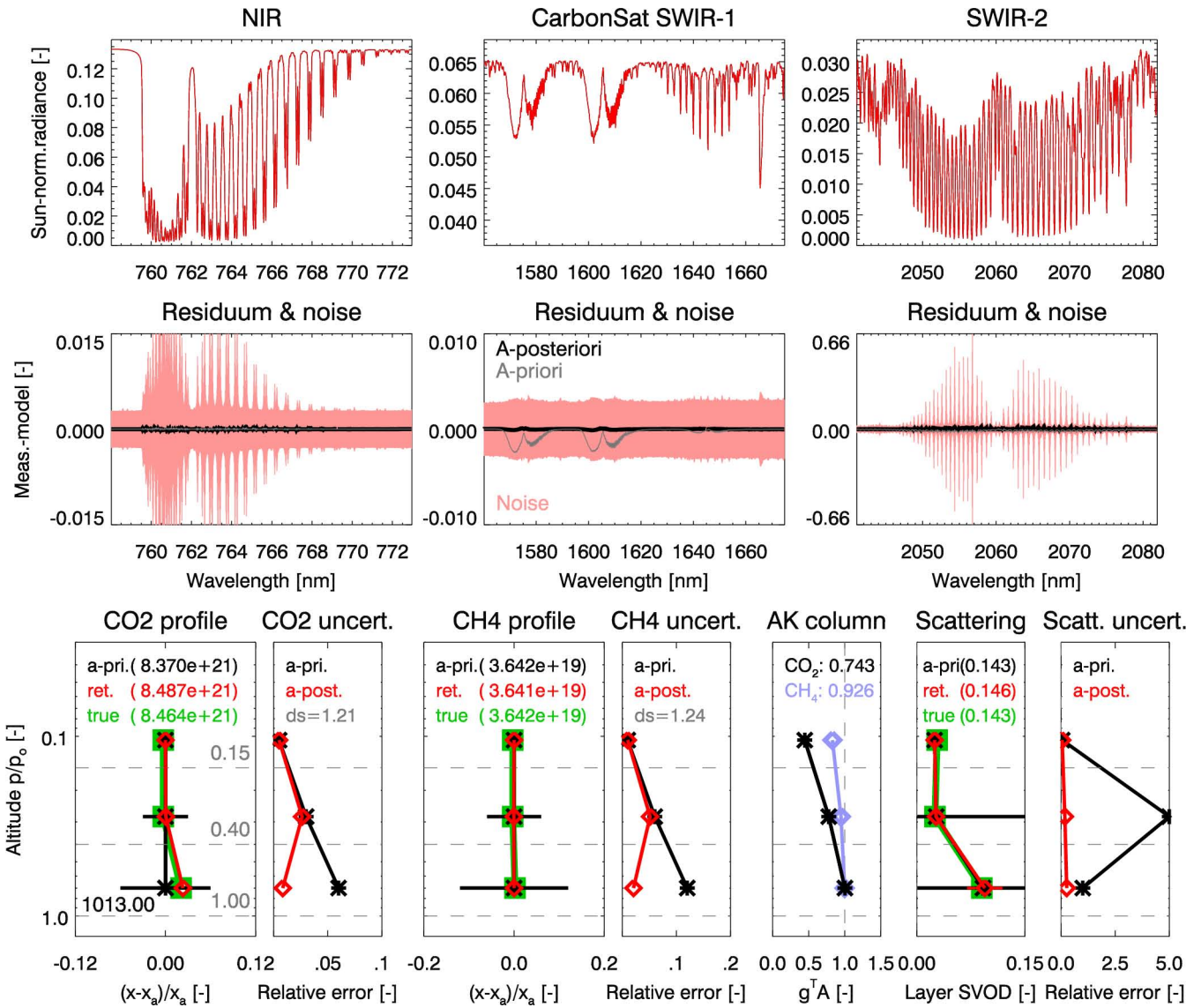


Fig. B2. Retrieval results for the VEG₅₀ scenario. Top: Sun-normalized radiance in the three CarbonSat spectral bands. Middle: fit residuum (black line), i.e., relative difference between the simulated measurement and the fitted RT model. Also shown is the measurement noise (light red) and the difference between the measurement and the simulated measurement before the fit (grey line). Bottom: Vertical profiles of (from left to right) CO₂ and its uncertainty, CH₄ and its uncertainty, CO₂ and CH₄ vertical column averaging kernels (AK), and the scattering layer vertical optical depth (the numerical values are the total scattering optical depth at 760 nm) and its uncertainty. The black horizontal bars denote the assumed a-priori uncertainties (1-sigma) in the three layers.

Defining matrix $\mathbf{R}=\mathbf{A}-\mathbf{1}$, where $\mathbf{1}$ is a unit matrix, allows to compute another matrix, which is important for characterizing the retrieval, namely the smoothing error covariance matrix

$$\hat{\mathbf{S}}_s = \mathbf{R}\mathbf{S}_{x_a}\mathbf{R}^T, \quad (\text{B10})$$

which quantifies errors caused by limited (final) vertical resolution of the instrument. The measurement noise contribution to the overall uncertainty is given by the measurement noise covariance matrix

$$\hat{\mathbf{S}}_{y,x} = \mathbf{G}\mathbf{S}_y\mathbf{G}^T. \quad (\text{B11})$$

Of interest for this study are the absolute values of the state vector elements and the absolute values of functions of the state vector elements, in particular the total column of CO₂ and its statistical error. As the state vector \mathbf{x} has been defined using normalized dimensionless relative quantities, transformations from relative quantities to absolute quantities have to be carried out. The absolute value of state vector element j , \hat{x}_j^a , is related to its relative value, \hat{x}_j , by the following relation (here the alternative notation \bar{x} is used for the a-priori

state vector, i.e., for \bar{x}_a , to avoid confusion with the the same letter a used for “a-priori” and “absolute”):

$$\hat{x}_j^a = \bar{x}_j^a(1 + \hat{x}_j). \quad (\text{B12})$$

This equation defines the transformation of the “relative state vector” \hat{x} to the corresponding “absolute state vector” \hat{x}^a .

It can also be shown that the averaging kernel matrix for the absolute state vector elements can be obtained from the averaging kernel matrix for the relative state vector elements as follows:

$$(\mathbf{A}^a)_{ij} = (\mathbf{A})_{ij} \frac{\bar{x}_i^a}{\bar{x}_j^a}. \quad (\text{B13})$$

The vertical column of, for example, CO₂, can be computed from the absolute state vector elements (i.e., layer columns), given above, and the total column operator \mathbf{g} , which can be defined as follows: $\mathbf{g}^T = [0, 0, 0, \dots, 1, 1, 1, \dots, 0, 0, 0]$, where $g_i = 1$ corresponds to state vector elements over which need to be summed to compute the total column (for CO₂ the indices of the state vector are $i=0, 1$, and 2, as can be seen from Table B1). All other elements of \mathbf{g} , over which should not be summed, need to be set to 0. This formulation of \mathbf{g} requires that the corresponding CO₂ state vector elements are absolute sub-columns in, e.g., molecules/cm², as otherwise their sum will not yield the total vertical column.

Using these definitions, several important quantities, which are needed to characterize the retrieval, can be computed:

The a-priori vertical column of a gas of interest, e.g., CO₂, in absolute units (e.g., molecules/cm²) is given by

$$\bar{v} = \mathbf{g}^T \bar{\mathbf{x}}^a. \quad (\text{B14})$$

The corresponding retrieved vertical column in absolute units is by

$$\hat{v} = \bar{v} + \mathbf{g}^T (\hat{\mathbf{x}}^a - \bar{\mathbf{x}}^a). \quad (\text{B15})$$

The corresponding vertical column total statistical error is

$$\sigma_v^2 = \mathbf{g}^T \hat{\mathbf{S}}_x^a \mathbf{g}. \quad (\text{B16})$$

The vertical column averaging kernel (a vector) is given by

$$\mathbf{a}_v^T = \mathbf{g}^T \mathbf{A}^a. \quad (\text{B17})$$

The vertical column smoothing error is

$$\sigma_{vs}^2 = \mathbf{g}^T \hat{\mathbf{S}}_s^a \mathbf{g} \quad (\text{B18})$$

and the vertical column measurement noise error is

$$\sigma_{vyx}^2 = \mathbf{g}^T \hat{\mathbf{S}}_{yx}^a \mathbf{g}. \quad (\text{B19})$$

Finally, the dry air column-averaged mixing ratio of CO₂, denoted X_{CO_2} , is computed from the retrieved CO₂ column (in molecules/cm²), denoted \hat{v}_{CO_2} , and the retrieved surface pressure (obtained from the retrieved pressure profile scaling

factor), \hat{p}_o (in hPa). The retrieved X_{CO_2} , denoted \hat{X}_{CO_2} (in ppm), is obtained as follows:

$$\hat{X}_{\text{CO}_2} = \frac{\hat{v}_{\text{CO}_2}}{C \hat{p}_o / 1013.0}. \quad (\text{B20})$$

C is a constant and given by $C = 10^{-6} \times 2.15 \times 10^{25}$. Factor 10^{-6} accounts for the conversion to ppm and 2.15×10^{25} is the assumed number of gaseous air molecules of dry air above a surface of area 1 cm² for a surface pressure of 1013 hPa.

The statistical uncertainty of the retrieved X_{CO_2} (in relative units), denoted $\sigma_{X_{\text{CO}_2}}^r$, is computed from the relative statistical uncertainties of the retrieved CO₂ column and surface pressure:

$$\sigma_{X_{\text{CO}_2}}^r = \sqrt{(\sigma_{\text{CO}_2} / \hat{v}_{\text{CO}_2})^2 + (\sigma_{p_o} / \hat{p}_o)^2}. \quad (\text{B21})$$

The statistical uncertainty of X_{CO_2} in absolute units (ppm) is given by (1-sigma):

$$\sigma_{X_{\text{CO}_2}} = \sigma_{X_{\text{CO}_2}}^r \times \hat{X}_{\text{CO}_2}. \quad (\text{B22})$$

The X_{CO_2} and its error computed using the formulas given above is referred to as “p_o-proxy method” in this manuscript.

The second method used in this manuscript to obtain X_{CO_2} is the “CH₄-proxy method”. For this method the corresponding formulas are:

$$\hat{X}_{\text{CO}_2}(\text{CH}_4) = \frac{\hat{v}_{\text{CO}_2}}{\hat{v}_{\text{CH}_4} / X_{\text{CH}_4}^{\text{apri}}}, \quad (\text{B23})$$

where \hat{v}_{CH_4} is the retrieved vertical column of methane and $X_{\text{CH}_4}^{\text{apri}}$ is the assumed a-priori dry air column-averaged mixing ratio of methane (obtained from, e.g., the model atmosphere used for the radiative transfer simulation). The corresponding statistical (relative) uncertainty is given by:

$$\sigma_{X_{\text{CO}_2}(\text{CH}_4)}^r = \sqrt{(\sigma_{\text{CO}_2} / \hat{v}_{\text{CO}_2})^2 + (\sigma_{\text{CH}_4} / \hat{v}_{\text{CH}_4})^2}. \quad (\text{B24})$$

Using analog formulas the corresponding result for methane, i.e., $\hat{X}_{\text{CH}_4} \pm \sigma_{X_{\text{CH}_4}}$, can be obtained.

To illustrate this, BESD retrieval results for one scenario, the VEG₅₀ scenario, (surface albedo: vegetation, SZA: 50°) are shown in Fig. B2. As can be seen, a significant uncertainty reduction relative to the assumed a-priori uncertainty has been achieved for the tropospheric layers, especially for the lowest tropospheric layer (the stratospheric layer is well constrained). The true CO₂ vertical column is 8.464×10^{21} molecules/cm², which is 1.1% higher than the a-priori column, which is 8.370×10^{21} molecules/cm². The retrieved CO₂ vertical column is 8.487×10^{21} molecules/cm², which is close to the true column. The difference is 0.27%, i.e., not zero, e.g., because of the smoothing error, which is 0.17% (1-sigma). The a-priori CO₂ column uncertainty is 3.63% and is reduced to 0.29% after the retrieval. The assumed a-priori surface pressure uncertainty is 3.0% and is

reduced to 0.06% after the fit. The a-posteriori X_{CO_2} uncertainty is 1.2 ppm. The degree of freedom for signal (ds) is 1.21 for the CO_2 column and 1.24 for the CH_4 column, which indicates that essentially only vertical column information on CO_2 and CH_4 is available. The CO_2 column averaging kernel is approximately unity for the lowest layer indicating that the observing system is sensitive to CO_2 changes in the lowest atmospheric layer, which is also true for CH_4 . The two panels at the bottom right, which show the results for the scattering profile, indicate significant uncertainty reduction with respect to the (aerosol and cloud) scattering parameters.

Acknowledgements. This study was funded by Wirtschaftsförderung Bremen (WFB) (KlimaMonitor project), DLR-Bonn (CarbonMon project), and ESA (ADVANSE project). We thank M. Wieser and C. Tobehn, OHB System AG, Bremen, for detailed CarbonSat orbit information and V. Mogulsky, B. Sang, and S. Hofer, Kayser-Threde GmbH, Munich, for preliminary CarbonSat instrument parameters. We thank NASA for the MODIS/Aqua data product (Collection 5, MYD35.L2 MODIS Level2 Cloud Mask data product obtained from <http://ladsweb.nascom.nasa.gov/data/search.html>) and ECMWF for meteorological data. We have used spectral surface albedos obtained from the ASTER Spectral Library through courtesy of the Jet Propulsion Laboratory (JPL), California Institute of Technology, Pasadena, California (copyright 1999, California Institute of Technology) and the Digital Spectral Library 06 of the US Geological Survey. Information on power plants has been obtained from the CARMA data base (<http://carma.org>) and information on anthropogenic CO_2 emissions of individual countries has been obtained from the BP data base (<http://www.bp.com>). We thank Dietmar Heinze, Vattenfall Europe Generation AG & Co. KG, Cottbus, Germany, for providing us with specific information on the actual emission of the power plant Schwarze Pumpe, Germany. We have used data from the Emission Database for Global Atmospheric Research (EDGAR), release version 4.0, <http://edgar.jrc.ec.europa.eu/>, 2009, courtesy European Commission, Joint Research Centre (JRC)/Netherlands Environmental Assessment Agency (PBL). We thank V. Velazco for helpful comments on a draft version of the manuscript. Last but not least we thank two anonymous referees for their comments on the AMTD version of this publication, which resulted in a significantly improved manuscript.

Edited by: R. Sussmann

References

- Ackerman, K. V. and Sundquist, E. T.: Comparisons of Two U.S. Power-Plant Carbon Dioxide Emissions Data Sets, *Environ. Sci. Technol.*, 42, 5688–5693, 2008.
- Ackerman, S. A., Holz, R. E., Frey, R., Eloranta, E. W., Madux, B. C., and McGill, M.: Cloud detection with MODIS. Part II: validation, *J. Atmos. Ocean. Tech.*, 25(7), 1073–1086, 2008.
- Ackerman, S., Strabala, K., Menzel, W., Frey, R., Coeller, C., and Gumley, L.: Discriminating clear sky from clouds with MODIS, *J. Geophys. Res.*, 103, 32141–32157, 1998.

- Aichinger, H. M.: 6. CO_2 -Monitoring-Fortschrittsbericht der Stahlindustrie in Deutschland, Stahlinstitut VDEh im Stahl-Zentrum, http://www.stahl-online.de/wirtschaft_und_politik/Umwelt_und_Energiepolitik/Energiepolitik/6_CO2-Monitoring-Fortschrittsbericht.pdf, 79, 2007 (in German).
- Allard, P., Carbonnelle, J., Dajčević, D., et al.: Eruptive and diffuse emissions of CO_2 from Mount Etna, *Nature*, 351, 387–391, 1991.
- Amediek, A., Fix, A., Ehret, G., Caron, J., and Durand, Y.: Airborne lidar reflectance measurements at 1.57 μm in support of the A-SCOPE mission for atmospheric CO_2 , *Atmos. Meas. Tech.*, 2, 755–772, doi:10.5194/amt-2-755-2009, 2009.
- Aumann, H. H., Gregorich, D., and Gaiser, S.: AIRS hyperspectral measurements for climate research: Carbon dioxide and nitrous oxide effects, *Geophys. Res. Lett.*, 32, L05806, doi:10.1029/2004GL021784, 2005.
- Baker, D. F., Bösch, H., Doney, S. C., O'Brien, D., and Schimel, D. S.: Carbon source/sink information provided by column CO_2 measurements from the Orbiting Carbon Observatory, *Atmos. Chem. Phys.*, 10, 4145–4165, doi:10.5194/acp-10-4145-2010, 2010.
- Barkley, M. P., Monks, P. S., Hewitt, A. J., Machida, T., Desai, A., Vinnichenko, N., Nakazawa, T., Yu Arshinov, M., Fedoseev, N., and Watai, T.: Assessing the near surface sensitivity of SCIAMACHY atmospheric CO_2 retrieved using (FSI) WFM-DOAS, *Atmos. Chem. Phys.*, 7, 3597–3619, doi:10.5194/acp-7-3597-2007, 2007.
- Bergamaschi, P., Frankenberg, C., Meirink, J. F., Krol, M., Villani, M. G., Houweling, S., Dentener, F., Dlugokencky, E. J., Miller, J. B., Gatti, L. V., Engel, A., and Levin, I.: Inverse modeling of global and regional CH_4 emissions using SCIAMACHY satellite retrievals, *J. Geophys. Res.*, 114, doi:10.1029/2009JD012287, 2009.
- Bergamaschi, P., Frankenberg, C., Meirink, J. F., Krol, M., Dentener, F., Wagner, T., Platt, U., Kaplan, J. O., Körner, S., Heimann, M., Dlugokencky, E. J., and Goede, A.: Satellite cartography of atmospheric methane from SCIAMACHY onboard ENVISAT: 2. Evaluation based on inverse model simulations, *J. Geophys. Res.*, 112, D02304, doi:10.1029/2006JD007268, 2007.
- Bloom, A. A., Palmer, P. I., Fraser, A., Reay, D. S., and Frankenberg, C.: Large-Scale Controls of Methanogenesis Inferred from Methane and Gravity Spaceborne Data, *Science*, 327, 5963, 322–325, doi:10.1126/science.1175176, 2010.
- Bösch, H., Toon, G. C., Sen, B., Washenfelder, R. A., Wennberg, P. O., Buchwitz, M., de Beek, R., Burrows, J. P., Crisp, D., Christi, M., Connor, B. J., Natraj, V., and Yung, Y. L.: Space-based near-infrared CO_2 measurements: testing the orbiting carbon observatory retrieval algorithm and validation concept using SCIAMACHY observations over Park Falls, Wisconsin, *J. Geophys. Res.*, 111, D23302, doi:10.1029/2006JD007080, 2006.
- Bovensmann, H., Burrows, J. P., Buchwitz, M., Frerick, J., Noël, S., Rozanov, V. V., Chance, K. V., and Goede, A.: SCIAMACHY – mission objectives and measurement modes, *J. Atmos. Sci.*, 56, 127–150, 1999.
- Bovensmann, H., Buchwitz, M., Burrows, J. P., Reuter, M., Krings, T., Gerilowski, K., Schneising, O., Heymann, J., Tretner, A., and Erzinger, J.: A remote sensing technique for global monitoring of power plant CO_2 emissions from space and related applications, *Atmos. Meas. Tech. Discuss.*, 3, 55–110, doi:10.5194/amtd-3-

- 55–2010, 2010.
- Bréon, F.-M. and Ciais, P.: Spaceborne remote sensing of greenhouse gas concentrations, *C R Geoscience*, 342, 412–424, 2010.
- Bril, A., Oshchepkov, S., and Yokota, T.: Retrieval of atmospheric methane from high spectral resolution satellite measurements: a correction for cirrus cloud effects, *Appl. Optics*, 48, 11, 2139–2148, doi:10.1364/AO.48.002139, 2009.
- Buchwitz, M., Rozanov, V. V., and Burrows, J. P.: A correlated-k distribution scheme for overlapping gases suitable for retrieval of atmospheric constituents from moderate resolution radiance measurements in the visible/near-infrared spectral region, *J. Geophys. Res.*, 105, 15247–15262, 2000a.
- Buchwitz, M., Rozanov, V. V., and Burrows, J. P.: A near infrared optimized DOAS method for the fast global retrieval of atmospheric CH₄, CO, CO₂, H₂O, and N₂O total column amounts from SCIAMACHY/ENVISAT-1 nadir radiances, *J. Geophys. Res.*, 105, 15231–15246, 2000b.
- Buchwitz, M., de Beek, R., Burrows, J. P., Bovensmann, H., Warneke, T., Notholt, J., Meirink, J. F., Goede, A. P. H., Bergamaschi, P., Körner, S., Heimann, M., and Schulz, A.: Atmospheric methane and carbon dioxide from SCIAMACHY satellite data: initial comparison with chemistry and transport models, *Atmos. Chem. Phys.*, 5, 941–962, doi:10.5194/acp-5-941-2005, 2005.
- Buchwitz, M., de Beek, R., Noël, S., Burrows, J. P., Bovensmann, H., Bremer, H., Bergamaschi, P., Körner, S., and Heimann, M.: Carbon monoxide, methane and carbon dioxide columns retrieved from SCIAMACHY by WFM-DOAS: year 2003 initial data set, *Atmos. Chem. Phys.*, 5, 3313–3329, doi:10.5194/acp-5-3313-2005, 2005.
- Buchwitz, M., de Beek, R., Noël, S., Burrows, J. P., Bovensmann, H., Schneising, O., Khlystova, I., Bruns, M., Bremer, H., Bergamaschi, P., Körner, S., and Heimann, M.: Atmospheric carbon gases retrieved from SCIAMACHY by WFM-DOAS: version 0.5 CO and CH₄ and impact of calibration improvements on CO₂ retrieval, *Atmos. Chem. Phys.*, 6, 2727–2751, doi:10.5194/acp-6-2727-2006, 2006.
- Buchwitz, M., Schneising, O., Burrows, J. P., Bovensmann, H., Reuter, M., and Notholt, J.: First direct observation of the atmospheric CO₂ year-to-year increase from space, *Atmos. Chem. Phys.*, 7, 4249–4256, doi:10.5194/acp-7-4249-2007, 2007.
- Buchwitz, M., Reuter, M., Schneising, O., Heymann, J., Bovensmann, H., and Burrows, J. P.: Towards an improved CO₂ retrieval algorithm for SCIAMACHY on ENVISAT, *Proceedings Atmospheric Science Conference, Barcelona, Spain, 7–11 September 2009*, ESA Special Publication SP-676, 2009.
- Burrows, J. P., Hölzle, E., Goede, A. P. H., Visser, H., and Fricke, W.: SCIAMACHY – scanning imaging absorption spectrometer for atmospheric cartography, *Acta Astronaut.*, 35(7), 445–451, 1995.
- Burrows, J. P., Bovensmann, H., Bergametti, G., Flaud, J. M., Orphal, J., Noël, S., Monks, P. S., Corlett, G. K., Goede, A. P., von Clarmann, T., Steck, T., Fischer, H., and Friedl-Vallon, F.: The geostationary tropospheric pollution explorer (GeoTROPE) mission: objectives, requirements and mission concept, *Adv. Space Res.*, 34, 682–687, 2004.
- Butz, A., Hasekamp, O. P., Frankenberg, C., and Aben, I.: Retrievals of atmospheric CO₂ from simulated space-borne measurements of backscattered near-infrared sunlight: accounting for aerosol effects, *Appl. Optics*, 48, 18, 3322–3336, doi:10.1364/AO.48.003322, 2009.
- Canadell, J. G., Le Quéré, C., Raupach, M. R., Field, C. B., Buitenhuis, E. T., Ciais, P., Conway, T. J., Gillett, N. P., Houghton, R. A., and Marland, G.: Contributions to accelerating atmospheric CO₂ growth from economic activity, carbon intensity, and efficiency of natural sinks, *Proceedings of the National Academy of Sciences (PNAS) of the United States of America*, 20 November 2007, 104, 18866–18870, 2007.
- Chédin, A., Hollingsworth, A., Scott, N. A., Serrar, S., Crevoisier, C., and Armante, R.: Annual and seasonal variations of atmospheric CO₂, N₂O and CO concentrations retrieved from NOAA/TOVS satellite observations, *Geophys. Res. Lett.*, 29, 1269, doi:10.1029/2001GL014082, 2002.
- Chédin, A., Serrar, S., Scott, N. A., Crevoisier, C., and Armante, R.: First global measurement of midtropospheric CO₂ from NOAA polar satellites: Tropical zone, *J. Geophys. Res.*, 108, 4581, doi:10.1029/2003JD003439, 2003.
- Chevallier, F., Engelen, R. J., and Peylin, P.: The contribution of AIRS data to the estimation of CO₂ sources and sinks, *Geophys. Res. Lett.*, 32, 23801, doi:10.1029/2005GL024229, 2005.
- Chevallier, F., Bréon, F.-M., and Rayner, P. J.: Contribution of the orbiting carbon observatory to the estimation of CO₂ sources and sinks: theoretical study in a variational data assimilation framework, *J. Geophys. Res.*, 112, D09307, doi:10.1029/2006JD007375, 2007.
- Ciais, P., Paris, J. D., Marland, G., P. Peylin, P., Piao, S. L., Levis, I., Pregger, T., Scholz, Y., Friedrich, R., Rivier, L., Houweling, S., Schulze, E. D., et al.: The European carbon balance. Part 1: fossil fuel emissions, *Glob. Change Biol.*, 16, 1395, doi:10.1111/j.1365-2486.2009.02098.x, 2010.
- Connor, B. J., Boesch, H., Toon, G., Sen, B., Miller, C., and Crisp, D.: Orbiting Carbon Observatory: Inverse Method and Prospective Error Analysis, *J. Geophys. Res.*, 113, D05305, doi:10.1029/2006JD008336, 2008.
- Crevoisier, C., Chédin, A., Matsueda, H., Machida, T., Armante, R., and Scott, N. A.: First year of upper tropospheric integrated content of CO₂ from IASI hyperspectral infrared observations, *Atmos. Chem. Phys.*, 9, 4797–4810, doi:10.5194/acp-9-4797-2009, 2009a.
- Crevoisier, C., Nobileau, D., Fiore, A. M., Armante, R., Chédin, A., and Scott, N. A.: Tropospheric methane in the tropics – first year from IASI hyperspectral infrared observations, *Atmos. Chem. Phys.*, 9, 6337–6350, doi:10.5194/acp-9-6337-2009, 2009b.
- Crisp, D., Atlas, R. M., Bréon, F.-M., Brown, L. R., Burrows, J. P., Ciais, P., Connor, B. J., Doney, S. C., Fung, I. Y., Jacob, D. J., Miller, C. E., O'Brien, D., Pawson, S., Rander-son, J. T., Rayner, P., Salawitch, R. S., Sander, S. P., Sen, B., Stephens, G. L., Tans, P. P., Toon, G. C., Wennberg, P. O., Wofsy, S. C., Yung, Y. L., Kuang, Z., Chudasama, B., Sprague, G., Weiss, P., Pollock, R., Kenyon, D., and Schroll, S.: The Orbiting Carbon Observatory (OCO) mission, *Adv. Space Res.*, 34, 700–709, 2004.
- Crisp, D., Miller, C., Bréon, F. M., Boesch, H., et al.: The Need for Atmospheric Carbon Dioxide Measurements from Space: Contributions from a Rapid Reflight of the Orbiting Carbon Observatory, http://www.nasa.gov/pdf/363474main.OCO_Reflight.pdf, p.54, 12 May 2009.
- Christi, M. J. and Stephens, G. L.: Retrieving profiles of atmospheric CO₂ in clear sky and in the presence of thin

- cloud using spectroscopy from the near and thermal infrared: a preliminary case study, *J. Geophys. Res.*, 109, D04316, doi:10.1029/2003JD004058, 2004.
- Dedikov, J. V., Akopova, G. S., Gladkaja, N. G., et al.: Estimating methane releases from natural gas production and transmission in Russia, *Atmos. Environ.*, 33, 3291–3299, 1999.
- Department of Energy and Environmental Protection Agency: Carbon Dioxide Emissions from the Generation of Electric Power in the United States, Washington, DC 20585 (DoE) and 20460 (EPA), July 2000, p.19, 2000.
- Engelen, R. J. and Stephens, G. L.: Information content of infrared satellite sounding measurements with respect to CO₂, *J. Appl. Meteorol.*, 43, 373–378, 2004.
- Engelen, R. J., Andersson, E., Chevallier, F., Hollingsworth, A., Matricardi, M., McNally, A. P., Thépaut, J.-N., and Watts, P. D.: Estimating atmospheric CO₂ from advanced infrared satellite radiances within an operational 4-D-Var data assimilation system: Methodology and first results, *J. Geophys. Res.*, 109, D19309, doi:10.1029/2004JD004777, 2004.
- Engelen, R. J. and McNally, A. P.: Estimating atmospheric CO₂ from advanced infrared satellite radiances within an operational 4-D-Var data assimilation system: Results and validation, *J. Geophys. Res.*, 109, D18305, doi:10.1029/2005JD005982, 2005.
- Feng, L., Palmer, P. I., Bösch, H., and Dance, S.: Estimating surface CO₂ fluxes from space-borne CO₂ dry air mole fraction observations using an ensemble Kalman Filter, *Atmos. Chem. Phys.*, 9, 2619–2633, doi:10.5194/acp-9-2619-2009, 2009.
- Frankenberg, C., Meirink, J. F., van Weele, M., Platt, U., and Wagner, T.: Assessing methane emissions from global spaceborne observations, *Science*, 308, 1010–1014, 2005.
- Frankenberg, C., Bergamaschi, P., Butz, A., Houweling, S., Meirink, J. F., Notholt, J., Petersen, A. K., Schrijver, H., Warneke, T., and Aben, I.: Tropical methane emissions: a revised view from SCIAMACHY onboard ENVISAT, *Geophys. Res. Lett.*, 35, L15811, doi:10.1029/2008GL034300, 2008.
- Frey, R. A., Ackerman, S. A., Liu, Y. H., Strabala, K. I., Zhang, H., Key, J. R., and Wang, X. G.: Cloud detection with MODIS. Part I: improvements in the MODIS cloud mask for collection 5, *J. Atmos. Ocean. Tech.*, 25(7), 1057–1072, 2008.
- Gerilowski, K., Tretner, A., Krings, T., Buchwitz, M., Bertagnolio, P. P., Belemzov, F., Erzinger, J., Burrows, J. P., and Bovensmann, H.: MAMAP – A new spectrometer system for column-averaged methane and carbon dioxide observations from aircraft: Instrument description and initial performance assessment, in preparation, 2010.
- Gloudemans, A. M. S., Schrijver, H., Kleipool, Q., van den Broek, M. M. P., Straume, A. G., Lichtenberg, G., van Hees, R. M., Aben, I., and Meirink, J. F.: The impact of SCIAMACHY near-infrared instrument calibration on CH₄ and CO total columns, *Atmos. Chem. Phys.*, 5, 2369–2383, doi:10.5194/acp-5-2369-2005, 2005.
- Gregg, J. S., Andres, R. J., and Marland, G.: China: emissions pattern of the world leader in CO₂ emissions from fossil fuel consumptions and cement production, *Geophys. Res. Lett.*, 35, L08806, doi:10.1029/2007GJ032887, 1–5, 2008.
- Gurney, K. R., Mendoza, D., Zhou, Y., Fischer, M., de la Rue du Can, S., Geethakumar, S., and Miller: The Vulcan Project: High resolution fossil fuel combustion CO₂ emissions fluxes for the United States, *Environ. Sci. Technol.*, 43, doi:doi:10.1021/es900806c, 2009.
- Hamazaki, T., Kaneko, Y., and Kuze, A.: Carbon dioxide monitoring from the GOSAT satellite, Proceedings XXth ISPRS conference, Istanbul, Turkey, 12–23 July 2004, p. 3, <http://www.isprs.org/proceedings/XXXV/congress/comm7/papers/43.pdf>, 2004.
- Houweling, S., Breon, F.-M., Aben, I., Rödenbeck, C., Gloor, M., Heimann, M., and Ciais, P.: Inverse modeling of CO₂ sources and sinks using satellite data: a synthetic inter-comparison of measurement techniques and their performance as a function of space and time, *Atmos. Chem. Phys.*, 4, 523–538, doi:10.5194/acp-4-523-2004, 2004.
- Houweling, S., Hartmann, W., Aben, I., Schrijver, H., Skidmore, J., Roelofs, G.-J., and Breon, F.-M.: Evidence of systematic errors in SCIAMACHY-observed CO₂ due to aerosols, *Atmos. Chem. Phys.*, 5, 3003–3013, doi:10.5194/acp-5-3003-2005, 2005.
- Solomon, S., Qin, D., Manning, M., Chen, Z., Marquis, M., Averyt, K. B., Tignor, M., and Miller, H. L.: *Climate Change 2007: The Physical Science Basis*, Contribution of Working Group I to the Fourth Assessment Report of the Intergovernmental Panel on Climate Change (IPCC), Cambridge University Press, 996 pp., 2007.
- Jagovkina, S. V., Karol, I. L., Zubov, V. A., Lagun, V. E., Reshetnikov, A. I., and Rozanov, E. V.: Reconstruction of the methane fluxes from the West Siberian gas fields by the 3-D regional chemical transport model, *Atmos. Environ.*, 34, 5319–5329, 2000.
- Judd, A.: Natural seabed gas seeps as sources of atmospheric methane, *Environ. Geol.*, 46, 988–996, 2004.
- Kourtidis, K., Kioutsioukis, I., McGinnis, D. F., and Rapsomanikis, S.: Effects of methane outgassing on the Black Sea atmosphere, *Atmos. Chem. Phys.*, 6, 5173–5182, doi:10.5194/acp-6-5173-2006, 2006.
- Krings, T., Buchwitz, M., Gerilowski, K., et al.: MAMAP – A new spectrometer system for column-averaged methane and carbon dioxide observations from aircraft: Retrieval algorithm and first inversions for point source emission rates, in preparation, 2010.
- Kuang, Z., Margolis, J., Toon, G., Crisp, D., and Yung, Y.: Space-borne measurements of atmospheric CO₂ by high-resolution NIR spectrometry of reflected sunlight: an introductory study, *Geophys. Res. Lett.*, 29, 1716, doi:10.1029/2001GL014298, 2002.
- Kulawik, S. S., Jones, D. B. A., Nassar, R., Irion, F. W., Worden, J. R., Bowman, K. W., Machida, T., Matsueda, H., Sawa, Y., Biraud, S. C., Fischer, M. L., and Jacobson, A. R.: Characterization of Tropospheric Emission Spectrometer (TES) CO₂ for carbon cycle science, *Atmos. Chem. Phys.*, 10, 5601–5623, doi:10.5194/acp-10-5601-2010, 2010.
- Kuze, A., Suto, H., Nakajima, M. and Hamazaki, T.: Thermal and near infrared sensor for carbon observation Fourier-transform spectrometer on the Greenhouse Gases Observing Satellite for greenhouse gases monitoring, *Appl. Optics*, 48, 35, 2009.
- Leifer, I., Roberts, D., Margolis, J., and Kinnaman, F.: In situ sensing of methane emissions from natural marine hydrocarbon seeps: A potential remote sensing technology, *Earth Planet. Sc. Lett.*, 245, 509–522, 2006a.
- Leifer, I., Luyendyk, B. P., Boles, J., and Clark, J. F.: Natural methane seepage blowout: contribution to atmospheric methane, *Global Biogeochem. Cy.*, 20, GB3008, doi:10.1029/2005GB002668, 1–9, 2006b.
- Masters, G. M.: *Introduction to Environmental Engineering and Science*, Prentice-Hall, Inc., 2nd edn., 413pp., 1998.

- Meirink, J. F., Eskes, H. J., and Goede, A. P. H.: Sensitivity analysis of methane emissions derived from SCIAMACHY observations through inverse modelling, *Atmos. Chem. Phys.*, 6, 1275–1292, doi:10.5194/acp-6-1275-2006, 2006.
- Meirink, J. F., Bergamaschi, P., and Krol, M. C.: Four-dimensional variational data assimilation for inverse modelling of atmospheric methane emissions: method and comparison with synthesis inversion, *Atmos. Chem. Phys.*, 8, 6341–6353, doi:10.5194/acp-8-6341-2008, 2008.
- Miller, C. E., Crisp, D., DeCola, P. L., Olsen, S. C., Randerson, J. T., Michalak, A. M., Alkhaled, A., Rayner, P., Jacob, D. J., Suntharalingam, P., Jones, D. B. A., Denning, A. S., Nicholls, M. E., Doney, S. C., Pawson, S., Boesch, H., Connor, B. J., Fung, I. Y., O'Brien, D. O., Salawitch, R. J., Sander, S. P., Sen, B., Tans, P., Toon, G. C., Wennberg, P. O., Wofsy, S. C., Yung, Y. L., and Law, R. M.: Precision requirements for space-based XCO₂ data, *J. Geophys. Res.*, 112, D10314, doi:10.1029/2006JD007659, 2007.
- National Research Council (NRC) – Committee on Methods for Estimating Greenhouse Gas Emissions, *Verifying Greenhouse Gas Emissions: Methods to Support International Climate Agreements*, ISBN 0-309-15212-7, 144 pages, prepublication version, available from <http://www.nap.edu/catalog/12883.html>, 2010.
- Oda, T. and Maksyutov, S.: A very high-resolution global fossil fuel CO₂ emission inventory derived using a point source database and satellite observations of nighttime lights, 1980–2007, *Atmos. Chem. Phys. Discuss.*, 10, 16307–16344, doi:10.5194/acpd-10-16307-2010, 2010.
- Oshchepkov, S., Bril, A., and Yokota, T.: PPDF-based method to account for atmospheric light scattering in observations of carbon dioxide from space, *J. Geophys. Res.*, 113, D23210, 12pp., doi:10.1029/2008JD010061, 2008.
- Palmer, P. I. and Rayner, P.: Atmospheric science: failure to launch, *Nature Geosci.*, 2, 247, doi:10.1038/ngeo495, 2009.
- Péré, J.-C., Pont, V., Mallet, M., and Bessagnet, B.: Mapping of PM₁₀ surface concentrations derived from satellite observations of aerosol optical thickness over South-Eastern France, *Atmos. Res.*, 91, pp. 1–8, doi:10.1016/j.atmosres.2008.05.001, 2009.
- Peters, W., Jacobson, A. R., Sweeney, C., Andrews, A. E., Conway, T. J., Masarie, K., Miller, J. B., Bruhwiler, L. M. P., Pétron, G., Hirsch, A. I., Worthy, D. E. J., van der Werf, G. R., Randerson, J. T., Wennberg, P. O., Krol, M. C., and Tans, P. P.: An atmospheric perspective on North American carbon dioxide exchange: CarbonTracker, *Proceedings of the National Academy of Sciences (PNAS) of the United States of America*, 27 November 2007, 104, 48, 18925–18930, 2007.
- Prasad, A. K., Singh, R. P., and Kafatos, M.: Influence of coal based thermal power plants on aerosol optical properties in the Indo-Gangetic basin, *Geophys. Res. Lett.*, 33, L05805, doi:10.1029/2005GL023801, pp.4, 2006.
- Rayner, P. J. and O'Brien, D. M.: The utility of remotely sensed CO₂ concentration data in surface inversions, *Geophys. Res. Lett.*, 28, 175–178, 2001.
- Rayner, P. J., Raupach, M. R., Paget, M., Peylin, P., and Koffi, E.: A new global gridded dataset of CO₂ emissions from fossil fuel combustion: Methodology and evaluation, *J. Geophys. Res.*, in press, 2010.
- Reuter, M., Buchwitz, M., Schneising, O., Heymann, J., Bovensmann, H., and Burrows, J. P.: A method for improved SCIAMACHY CO₂ retrieval in the presence of optically thin clouds, *Atmos. Meas. Tech.*, 3, 209–232, doi:10.5194/amt-3-209-2010, 2010.
- Rodgers, C. D.: *Inverse Methods for Atmospheric Sounding: Theory and Practice*, World Scientific Publishing, 2000.
- Rodgers, C. D. and Connor, B. J.: Intercomparison of remote sounding instruments, *J. Geophys. Res.*, 108(D3), 2003.
- Rozanov, V. V., Buchwitz, M., Eichmann, K.-U., de Beek, R., and Burrows, J. P.: SCIATRAN – a new radiative transfer model for geophysical applications in the 240–2400 nm spectral region: the pseudo-spherical version, *Adv. Space Res.*, 29, 1831–1835, 2002.
- Schneising, O., Buchwitz, M., Burrows, J. P., Bovensmann, H., Reuter, M., Notholt, J., Macatangay, R., and Warneke, T.: Three years of greenhouse gas column-averaged dry air mole fractions retrieved from satellite – Part 1: Carbon dioxide, *Atmos. Chem. Phys.*, 8, 3827–3853, doi:10.5194/acp-8-3827-2008, 2008.
- Schneising, O., Buchwitz, M., Burrows, J. P., Bovensmann, H., Bergamaschi, P., and Peters, W.: Three years of greenhouse gas column-averaged dry air mole fractions retrieved from satellite – Part 2: Methane, *Atmos. Chem. Phys.*, 9, 443–465, doi:10.5194/acp-9-443-2009, 2009.
- Shindell, D. and Faluvegi, G.: The net climate impact of coal-fired power plant emissions, *Atmos. Chem. Phys.*, 10, 3247–3260, doi:10.5194/acp-10-3247-2010, 2010.
- Shakhova, N., Semiletov, I., Salyuk, A., Yusupov, V., Kosmach, D., and Gustafsson, O.: Extensive Methane Venting to the Atmosphere from Sediments of the East Siberian Arctic Shelf, *Science*, 327, doi:10.1126/science.1182221, 1246–1250, 2010.
- Siddique, T., Gupta, R., Fedorak, P. M., MacKinnon, M. D., and Foght, J. M.: A first approximation kinetic model to predict methane generation from an oil sands tailings settling basin, *Chemosphere* 72, 1573–1580, 2008.
- Strow, L. L., Hannon, S. E., De-Souza Machado, S., Motteler, H. E., and Tobin, D. C.: Validation of the atmospheric infrared sounder radiative transfer algorithm, *J. Geophys. Res.*, 111, D09S06, doi:10.1029/2005JD006146, 2006.
- Sutton, O. G.: *A Theory of Eddy Diffusion in the Atmosphere*, *Proceedings of the Royal Society of London, Series A, Containing Papers of a Mathematical and Physical Character*, The Royal Society of London, London, UK, 135(826), 143–165, 1932.
- Villasenor, R., Magdaleno, M., Quintanar, A., Gallardo, J., C., Lopez, M. T., Jurado, R., Miranda, A., Aguilar, M., Melgarejo, L. A., Palmerin, E., Vallejo, C. J., and Barchet, W. R.: An air quality emission inventory of offshore operations for the exploration and production of petroleum by the Mexican oil industry, *Atmos. Environ.*, 37, 3713–3729, 2003.
- Westbrook, G. K., Thatcher, K. E., Rohling, E. J., et al.: Escape of methane from the seabed along West Spitsbergen continental margin, *Geophys. Res. Lett.*, 36, L15608, doi:10.1029/2009GL039191, 2009.